BULETINUL INSTITUTULUI POLITEHNIC DIN IAŞI

Volumul 62 (66)
Numărul 4

Secția
MATEMATICĂ
MECANICĂ TEORETICĂ
FIZICĂ

2016 **Editura POLITEHNIUM**

BULETINUL INSTITUTULUI POLITEHNIC DIN IAŞI
PUBLISHED BY
"GHEORGHE ASACHI" TECHNICAL UNIVERSITY OF IAŞI
Editorial Office: Bd. D. Mangeron 63, 700050, Iaşi, ROMANIA
Tel. 40-232-278683; Fax: 40-232-237666; e-mail: polytech@mail.tuiasi.ro

BULETINUL INSTITUTULUI POLITEHNIC DIN IAŞI
BULLETIN OF THE POLYTECHNIC INSTITUTE OF IAŞI
Volumul 62 (66), Numărul 4 2016

Secția

MATEMATICĂ. MECANICĂ TEORETICĂ. FIZICĂ

SUMAR

BULETINUL INSTITUTULUI POLITEHNIC DIN IAŞI
BULLETIN OF THE POLYTECHNIC INSTITUTE OF IAŞI
Volume 62 (66), Number 4 2016

Section

MATHEMATICS. THEORETICAL MECHANICS. PHYSICS

CONTENTS

BULETINUL INSTITUTULUI POLITEHNIC DIN IAŞI
Publicat de
Universitatea Tehnică „Gheorghe Asachi” din Iaşi
Volumul 62 (66), Numărul 4, 2016
Secţia
MATEMATICĂ. MECANICĂ TEORETICĂ. FIZICĂ

IMPEDANCE CHARACTERIZATION OF A DEEP BRAIN STIMULATING ELECTRODE: TRANSIENT PULSE RESPONSE

BY

BOGDAN NEAGU[1] and EUGEN NEAGU[2,3,*]

[1]Toronto Western Research Institute, University Health Network and Division of Neurology, Department of Medicine, University of Toronto, Toronto, Canada
[2]Universidade Nova de Lisboa, Caparica, Portugal, Departamento de Ciência dos Materiais
[3]“Gheorghe Asachi” Technical University of Iaşi, Department of Physics

Received: November 18, 2016
Accepted for publication: December 16, 2016

Abstract. The goal of this study was to present an analytical equation for the instantaneous electrical impedance $Z(t)$ of the electrode for the case when it is used with pulsed current of similar values with those used for clinical applications. $Z(t)$ increases with time t being proportional with $t^{0.9}$. It decreases with increasing voltage U, increasing current I and decreasing resistivity ρ. We propose an equation for $Z(t)$ for different values of I and ρ ($Z_{I,\rho}(t)$). This equation is used to calculate the patient-specific parameters of interest, *i.e.*, the voltage necessary to inject a certain current, the delivered charge, the electrical efficiency of the electrode, etc., as function of time for specific conditions. For the same applied voltage, the delivered charge and the electrical efficiency are little higher for monopolar configuration than for bipolar configuration but the difference decreases as ρ increases.

Keywords: deep brain stimulation; instantaneous electrical impedance; pulsed current.

[*]Corresponding author; *e-mail*: euneagu1@yahoo.com

1. Introduction

Over the last two decades deep brain stimulation (DBS) has evolved from an experimental technology to a well-established surgical therapy for numerous disorders (Miocinovic *et al*., 2013; Shah *et al*., 2010; Hariz *et al*., 2013). Present day implantable pulse generator (IPG) units and external trial stimulators for DBS applications deliver biphasic, charge-balanced pulse-pair trains as advocated by Lilly nearly a half century ago (Lilly, 1961). The maximum amplitude and pulse width of IPG unit are 10.5 V and 450 ms. The Medtronic 3387 DBS electrode is used with pulsed voltage or pulsed current, in the range of 1-8 V (0.1–2 mA), 60–180 μs pulse width, and 100–185 pulses per second (Coffey, 2008). Optimal selection of stimulation parameters remains a challenge.

An accurate description of the DBS electrode impedance is important for *in vivo* applications (*i.e.* stimulation, electrode-tissue interface characterization, brain tissue characterization, the formation of the encapsulation layer, field potential recording, etc.) and for the development of computational models of neural recording and stimulation that aim to improve the understanding of neuro–electric interfaces and electrode design.

There is little information about the Medtronic 3387 DBS electrode impedance characterization with pulsed signal (Wei and Grill, 2009) or with pulsed signal of clinical relevance (Holsheimer *et al*., 2009). We don't have an analytical equation for the electrode impedance as function of time, current or voltage and saline resistivity. Detailed characterization of the impedance of the electrode is required for the accurate calculation of the current passing through the tissue and the charge delivered to the brain for given stimulation conditions. This may facilitate the selection of optimal stimulation parameters. The average value of the impedance reported for patients was 1200 Ω (range: 415–1999 Ω) (Coffey, 2008). As a safety feature, the programming device calculates the charge density based on a conservative impedance value of 500 Ω. No distinction is made between the electrical impedance of the brain tissue, as part of the electrode impedance, and the total impedance of the electrode which include as well the impedance of the connecting leads and of the metal-tissue interface. Consequently the voltage applied on the tissue is significantly lower than the voltage applied on the DBS electrode. The experimental measurements show that the electrode impedance is time, voltage, current and saline concentration (electrical resistivity) dependent (Wei and Grill, 2009; Lempka *et al*., 2009). Consequently it is opportune to find an analytical equation for the instantaneous impedance of the DBS electrode as function of the above parameters.

The goal of this study was to present a simple quantitative analytical model for the electrical impedance of the Medtronic 3387 DBS electrode using pulsed current of similar values with those used for *in vivo* applications. An analytical equation for the electrode impedance as function of time, current and saline resistivity is given.

2. Methods

The impedance properties for two adjacent contacts (bipolar configuration) of the Medtronic 3387 DBS electrode showed in Fig. 1*a* were measured. Two contacts were specifically used to make available two metal-saline interfaces. Thus the contribution of the impedance of the two interfaces was relevant by comparison to other contributions (*e.g.*, saline impedance and the coupling capacitance between the leads).

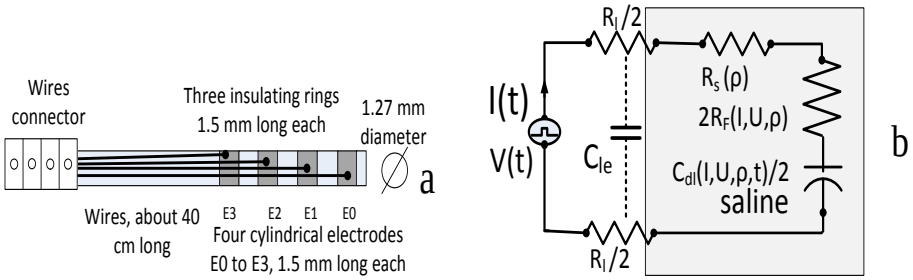

Fig. 1 – (*a*) The Medtronic 3387 electrode for deep brain stimulation; (*b*) The equivalent circuits of the DBS electrode for the case of bipolar configuration.

Measurements were performed in a tank filled with 2 l saline, placed in a Faraday cage, of different concentrations (1-9 NaCl gl^{-1}, electrical resistivity ρ from 5.025 to 0.625 Ωm) at 23ºC. The voltage transients generated by applying clinically relevant positive pulse currents (200 μs width and 20 ms repetition period, if not otherwise specified) were measured at 7 current amplitudes from 0.15 mA to 2 mA. The experimental setup was similar with that used in literature (Holsheimer *et al*., 2009). The voltages were measured using a double-beam digital oscilloscope Agilent DSOX4022A, sample interval 0.1 μs, and transferred to a computer for storage and analysis. The measurements were replicated six times at 4 min time interval, if not otherwise stated, at each amplitude level and the average data are presented. The instantaneous impedance $Z(I,\rho,t)$ was calculated as the ratio between the instantaneous voltage and the instantaneous current.

The saline impedance R_s was previously approximated (Holsheimer *et al*., 2009) with the asymptotic impedance of the DBS electrode for pulse width ≈ 0 s or as the asymptotic high frequency impedance (Wei and Grill, 2009) (the metal-electrolyte impedance was modeled as a parallel *RC* circuit). To discriminate between metal-electrolyte impedance and bulk (saline) impedance, we calculated R_s and the geometry factor (*GF*) using simulations. For bipolar configuration a 2D axisymmetric finite element models of the DBS electrode and its surrounding medium were created.

2.1. Data Analysis

The series *RC* equivalent is at the heart of the behavior of an electrode-electrolyte interface. This equivalent does not account for the very-low-frequency behavior of the interface (Geddes, 1997). Various equivalent circuits have been suggested in an effort to better reproduce the electrode-saline interface response (Geddes, 1997; Schwan, 1968; de Boer, 1978). We will use a simple electrical circuit presented in Fig. 1*b* and will show that for the experimental conditions of interest for clinical use of the DBS electrode, the experimental data can be analyzed using this model. The coupling capacitance C_{le} between the metallic leads running from the DBS electrode connector to the cylindrical contacts will be neglected. We assume that the two metal-saline interfaces have the same characteristics and the equivalent circuit reduces to $(R_l + R_S(\rho)+2R_F(U,I,\rho))$ in series with $C_{dl}(U,I,\rho,t)/2$, where R_l is the resistance determined by the length of the metallic leads between the DBS electrode connector and the cylindrical contacts, $R_S(\rho)$the resistance of the saline, $R_F(U,I,\rho)$ the faradaic resistance at metal-saline interface, and $C_{dl}(U,I,\rho,t)$ a time-dependent double layer capacitance at metal-saline interface. If $U(t)$ is the applied voltage and $I(t)$ is the current passing through the circuit, we have:

$$U(t) = I(t)(R_l + R_s(\rho) + 2R_F(I,\rho)) + \frac{2\,Q(t)}{C_{dl}(I,\rho,t)} \tag{1}$$

where Q(t) is the electric charge on the double layer capacitance at interface:

$$Q(t) = \int_0^t I(t)dt \tag{2}$$

For a constant-current stimulation Eq. (2) reads:

$$Q(t) = It \tag{3}$$

From Eq. (1) it results:

$$U(t) = I(R_l + R_s(\rho) + 2R_F(I,\rho)) + \frac{2\,It}{C_{dl}(I,\rho,t)} \tag{4}$$

We will assume that for short time the double layer capacitance increases with time as:

$$C_{dl}(t) = C_{dl0}t^m \tag{5}$$

where C_{dl0}, units Fs^{-m}, was a measure of the double layer capacitance at 1 second and m was a measure of the deviation from pure capacitive (m = 0) behavior. It results:

$$U(t) = I(R_l + R_s(\rho) + 2R_F(I,\rho) + \frac{2\,t^{1-m}}{C_{dl\,0}(I,\rho)}) \quad (6)$$

and the instantaneous impedance of the DBS electrode is:

$$Z(I,\rho,t) = R_l + R_s(\rho) + 2R_F(I,\rho) + \frac{2\,t^{1-m}}{C_{dl\,0}(I,\rho)} \quad (7)$$

The experimental data obtained for values of I, ρ and t relevant for clinical applications of the DBS electrode are very well described if m = 0.1. The validity of Eq. (7) for m = 0 was verified by carrying out measurements on a lamped impedance network built from a resistors and a capacitor in series whose value has been (separately) determined by an impedance analyzer (Agilent 4294A). By fitting the experimental data to Eq. (7) the values for R and C were determined with errors below 0.3%.

3. Results

The resistance R_l of the 2×40 cm long metallic leads was measured with the contacts E1 and E2 short-circuited. It was 86.4 ± 0.3 Ω (mean value and standard deviation (SD)), comparable with the results from literature (Wei and Grill, 2009; Holsheimer *et al*., 2009). R_s of the saline involving contacts E1 and E2 was calculated using simulations. The result for 0.9% NaCl was R_s = 108 ± 3 Ω (mean value and SD for 13 simulation at different constant currents from 0.15 mA to 2 mA. This value is higher than the asymptotic value of ≈ 88 Ω reported for pulse width ≈ 0 s (Holsheimer *et al*., 2009). It is lower that the value (mean ± SD = 133 ± 7 Ω) estimated from the voltage transient responses to symmetrical biphasic square current pulses (Wei and Grill, 2009). From simulations for different electrical resistivity ρ from 0.625 to 10 Ωm, the geometry factor of the DBS electrode for bipolar configuration was calculated as:

$$GF = \frac{\rho}{R_s} \quad (8)$$

The value was GF = (0.0058 ± 0.0001) m, in good agreement with the value reported in literature (Vinter *et al*., 2009). In the case of monopolar stimulation, the IPG placed in the chest is used as reference electrode. The geometry of the connection between the head and neck, the geometry of the neck and of the connection between the neck and chest is complex and it consists of materials with very different electrical resistivity. For this reason we did not made simulations for the case of monopolar configuration and we used

data from AC measurements (Neagu and Neagu, 2016). The geometry factor for monopolar configuration was estimated as GFm = 0.0049 m.

3.1. Constant-Current Stimulation

Fig. 2 shows the instantaneous impedance for the DBS electrode as function of time for the case of stimulation with constant-current of 0.15, 1.2 and 2 mA in 0.9% saline solution. The impedance decreases as the current increases. The experimental data have been fitted to Eq. (7) to determine $R_F(I)$ and $C_{dl0}(I)$. The fitting curves are showed by lines superimposed on the symbols in Fig. 2.

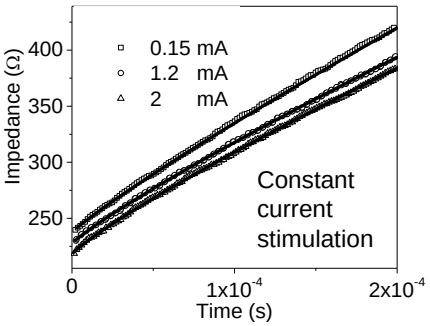

Fig. 2 – The instantaneous impedance as function of time The data have been fitted to Eq. (7) to determine $R_F(I)$ and $C_{dl0}(I)$. The fitting curves are showed by lines superimposed on the symbols.

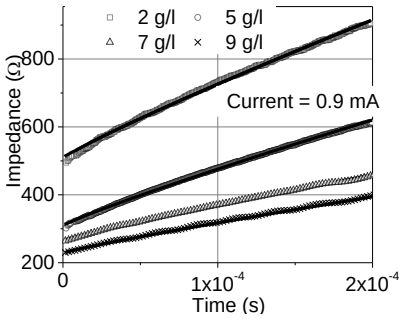

Fig. 3 – The instantaneous impedance as function of time for the DBS electrode in saline with different resistivity. The data have been fitted to Eq. (7) to determine $R_F(\rho)$ and $C_{dl0}(\rho)$.

Table 1

The Values Obtained for $R_F(I)$ and $C_{dl0}(I)$ by Fitting the Experimental Data for a Saline Resistivity ρ = 0.625 Ωm (0.9% NaCl) and Different Stimulating Currents to Eq. (7) with m = 0.1

Current, [mA]	0.15	0.34	0.68	0.9	1.2	2
R_F, [Ω]	21.4	20.4	19.7	18.8	17.3	12.9
C_{dl0}, [μFs^{-m}]	5.06	5.12	5.26	5.41	5.56	5.68

The fitting is very good, indicating that the theoretical model is appropriate. In fact, for a parallel circuit and $t \approx 0$ s R_F is shunted by C_{dl} and the impedance will be $Z(0) = R_s + R_l$ = 194.4 Ω. This value is lower than the experimental values in Fig. 2 indicating that the experimental data are not well described by a parallel equivalent circuit. Because we know R_s from simulation it results that the series circuit is appropriate to describe the experimental data.

The parameter values are presented in Table 1. As the current increases, R_F decreases and C_{dl0} increases in good agreement with data in literature (Wei and Grill, 2009; Schwan, 1968; Weinman and Mahler, 2010).

Fig. 3 shows the instantaneous impedance as function of time for the DBS electrode in saline with different resistivity of 2.631, 1.086, 0.793 and 0.625 Ωm, *i.e.*, for NaCl concentration of 2, 5, 7 and 9 gl^{-1} respectively. The data are for a current of 0.9 mA. As the saline resistivity decreases the impedance decreases. $R_s(\rho)$ was determined using Eq. (8). The experimental data have been fitted to Eq. (7) to determine $R_F(\rho)$ and $C_{dl0}(\rho)$. The fitting curves are showed by lines superimposed on the symbols in Fig 3. The fitting is very good, indicating that the theoretical model is appropriate. Parameter values are presented in Table 2.

Table 2
The Values Obtained for $R_F(\rho)$ and $C_{dl0}(\rho)$ by Fitting the Experimental Data for I = 0.9 mA and Different Saline Resistivity to Eq. (7) with m = 0.1

Resistivity, [Ωm]	5.025	2.631	1.821	1.086	0.793	0.625
R_F, [Ω]	60	44	32.9	23.3	21	17.8
C_{dl0}, [μFs^{-m}]	0.82	1.31	2.29	3.01	4.85	5.59

As the saline resistivity decreases $R_F(\rho)$ decreases and $C_{dl0}(\rho)$ increases, as expected.

4. Discussion

Data in Tables 1 to 2 will be used to obtain an analytical equation for the instantaneous impedance of the DBS electrode for experimental conditions of interest for clinical applications. This means that we will deduce an analytical equation of the instantaneous impedance $Z_{I,\rho}(t)$ for different values of the stimulation current and the electrical resistivity of the medium. Consequently, knowing I and ρ, the instantaneous impedance or other quantities related with it (*e.g.*, electrical charge delivered for certain conditions, the current injected, etc.) can be calculated.

4.1. Analytical Equation for the Instantaneous Impedance

Eq. (7) shows that in order to get an analytical equation for the instantaneous impedance we need to estimate $R_F(I,\rho)$ and $C_{dl0}(I,\rho)$. The variables I and ρ are independent variables. Taylor series is a representation of a function as an infinite sum of terms that are calculated from the values of the function's derivatives at a single point. We will expand $f(x,y)$ (*e.g.*, $R_F(x,y)$ or $C_{dl0}(x,y)$ were x is I and y is ρ), in Taylor series around a point (x_0, y_0). Because

the variation range of R_F and C_{dl0} with I and ρ is low, the series will be truncated after the second term:

$$f(x,y) \approx f(x_0,y_0) + (x-x_0)f_x(x_0,y_0) + (y-y_0)f_y(x_0,y_0) + \cdots + \quad (9)$$

where f_x and f_y denote the respective partial derivatives. Data in Tables 1 and 2 will be used to obtain $f(x_0,y_0)$ and the partial derivatives as function of I and ρ.

By fitting the data in Table 1, first row, with a line $R_F(I) = a - sI$, we obtain a = (22.6 ± 0.5) Ω and s = (4623 ± 401) ΩA^{-1}. By fitting the data in Table 2, first row, with a line it results $R_F(\rho) = a + s\rho$ with a = (14.8 ±2.1) Ω and s = (9.6 ± 0.8) m^{-1}. We will choose $x = I,\ y = \rho, x_0 = I_0 = 9 \times 10^{-4}$A and $y_0 = \rho_0 = 0.625$ Ωm. $R_F(I_0,\rho_0)$ = (18.8 + 17.8)/2 = 18.3 Ωm and we get:

$$R_F(I,\rho) \cong 18.3 + (I - 0.0009)(-4623) + (\rho - 0.625)9.6 + \cdots + \quad (10)$$

Similarly, from data in Table 1, second row, we have $C_{dl0}(I) = a + sI$, with a = (5.05 ± 0.06)×10^{-6} Fs$^{-0.1}$ and s = (3.4 ± 0.4)×10^{-6} Fs$^{-0.1}$A^{-1}. Electrochemical impedance measurements show that specific capacitance values for bright Pt are typically in the range of 10–30 μFcm^{-2} (Franks, 2005; Morgan *et al*., 2007). Assuming that I is very low, as in the case of electrochemical impedance measurements, and t = 100 μs, from Eq. (5) we get for the specific capacitance 33.5 μFcm^{-2} (the geometrical area of a cylindrical contact is 0.06 cm^{-2}) in good agreement with data in literature (Franks, 2005; Morgan *et al*., 2007).

The variation of C_{dl0} with ρ is nonlinear and can be described assuming $C_{dl0}(\rho)=b\rho^c$ with b and c constants. By fitting the data in Table 2, second row, we obtain $C_{dl0}(\rho)$ = 3.65×10$^{-6}\rho^{-0.95}$. The standard error of b and c is lower than 10%. We will choose $I_0 = 9 \times 10^{-4}$A and $\rho_0 = 0.625$ Ωm. $C_{dl0}(I_0,\rho_0)$ = (5.41 + 5.59) ×10^{-6}/2 = 5.5×10^{-6} Fs$^{-0.1}$ and we get:

$$C_{dlo}(I,\rho) \cong 5.5 \times 10^{-6} + (I - 0.0009)3.7 \times 10^{-4} + \\ +(\rho - 0.625)(-3.47 \times 10^{-6}\rho^{-1.95}) + \cdots + . \quad (11)$$

It results:

$$Z_{I\rho}(t) = R_l + \frac{\rho}{GF} + 2R_F(I,\rho) + 2\frac{t^{0.9}}{C_{dl\,0}(I,\rho)} \quad (12)$$

where $R_F(I,\rho)$ is given by Eq. (10) and $C_{dl0}(I,\rho)$ is given by Eq. (11). Eq. (12) allows us to calculate the instantaneous impedance for different I and different ρ. Fig. 4 shows the impedance at t = 50 μs for I in the range of 0.1- 4 mA and ρ in the range of 0.4-10 Ωm. $Z_{I\rho}(5\times10^{-5})$ varies in the range 200 to 2100 Ω. This interval is a little larger than the interval reported for patients (range: 415–1999 Ω)

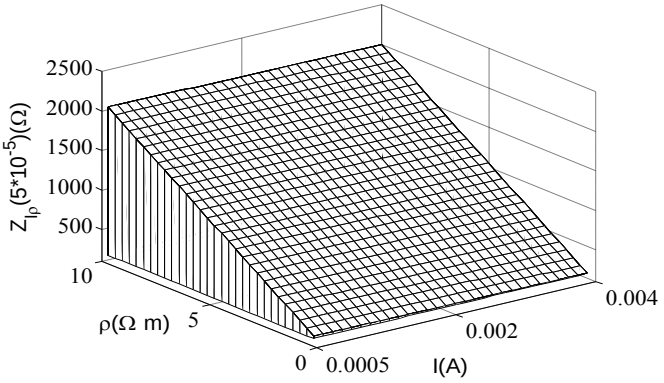

Fig. 4 – The calculated impedance at t = 50 μs for I in the range of 0.1- 4 mA and ρ in the range of 0.4-10 Ωm.

(Coffey, 2008) because the ranges for the two parameters I and ρ are larger. It is known that the safety limit of the charge density is below 30 μCcm^{-2}/ph (Coffey, 2008). For a pulse width of 100 μs the maximum safety current is 18 mA. Eq. (12) allows us to calculate the necessary voltage to inject a certain current for different ρ. The result for t = 100 μs is showed in Fig. 5 for bipolar configuration. The injected current is higher than the maximum safety limit of 18 mA only if ρ is low and U is high.

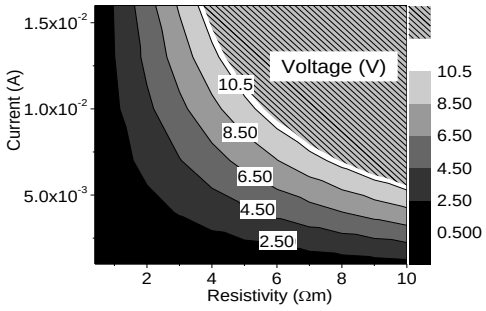

Fig. 5 – The necessary voltage to inject a certain current for different ρ and t = 100 μs.

4.2. Electrical Efficiency of the DBS Electrode

We propose that the electrical (energy) efficiency of the electrode during the stimulation process can be characterized by the ratio between the voltage drop on the saline and the voltage U_{ap} applied on the DBS electrode.

The voltage drop on saline is:

$$U_s(I, \rho, t) = IR_s(\rho) \tag{13}$$

The electrical efficiency $\eta(I, \rho, t)$ for a constant current I is:

$$\eta(I, \rho, t) = \frac{U_s(I,\rho,t)}{U_{ap}} = \frac{R_s(\rho)}{Z(I,\rho,t)} \tag{14}$$

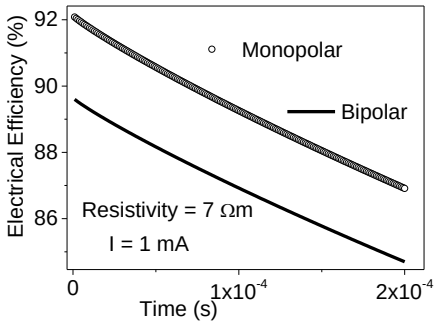

Fig. 6 – The electrical efficiency as function of time.

Eq. (14) shows how much of the applied voltage will spread in the tissue and eventually contribute to stimulation. Fig. 6 shows the electrical efficiency calculated for 1 mA and ρ = 7 Ωm. The line is for bipolar configuration and the circles for monopolar configuration. Electrical efficiency decreases as the time increases. The efficiency will decrease if other series resistances at the electrode-tissue interface are taken into account such as the encapsulation layer at the surface of the contacts or of the IPG. Finding solutions to decrease R_l, R_F and C_{dl} seems reasonable in order to increase the electrical efficiency of the DBS electrode.

4.3. Clinical Relevance of the Results

Detailed characterization of the instantaneous impedance of the DBS electrode may facilitate the selection of better stimulation parameters reducing the occurrence of side-effects. Data reported for patients in literature are not correlated with the applied voltage, the current or time. As a safety feature, the programming device calculates the charge density based on a conservative impedance value of 500 Ω. A proper knowledge of injected current and/or injected charge density is important for a better understanding of the physiological effect of the electrical stimulation.

The electrical (energy) efficiency of the electrode during the stimulation process can be calculated using Eq. (14). This will allow to find a better correlation between the voltage applied and the physiological response.

Knowing the *GF* and the tissue mean resistivity, the tissue resistance can be calculated using Eq. (8). For example, for white matter ρ = 7 Ωm (mean value) (Haueisen *et al*., 1997) and, consequently, using Eq. (8) the white matter resistance is 1209 Ω (bipolar configuration). It is significantly lower that the electrode impedance. This means that only a part of the voltage applied on the DBS electrode is applied on the nervous tissue and only this voltage is responsible for the physiological response.

In the case of monopolar configuration the high resistivity materials at the connection between head and neck, neck and the connection between neck and chest are of particular importance. Simulations shows that only 50% of the electrical impedance between the active contact and the IPG placed in the chest is determined by the brain tissue contained in a cylinder around the active contact with a radius of 12 mm and a height of 1.5 mm, in good agreement with data in literature (Walckiers *et al*., 2010). In the case of monopolar stimulation, because the resistance is spread over a large volume, an increase of the electrical efficiency does not necessarily means an increase of the volume of the activated tissue. The activation of a neuron by an extracellular stimulation is linked to the value of the double spatial derivative of the electrical potential along the fiber direction (Rattay, 1989). It is known that the use of a IPG implanted in the chest as reference electrode leads to an increase of the electrode impedance (+48%) and a reduction of the area of activated tissue (−15%) (Rattay). It is obvious that the stimulated volume is almost double in the case of bipolar configuration when higher voltage drop is expected around the two active contacts.

5. Conclusions

An analytical equation is proposed for the Medtronic 3387 DBS electrode impedance as function of time, current and saline resistivity of similar values with those used for clinical applications. This equation should be used to calculate the parameters of interest, *i.e*., the necessary voltage to inject a certain current, the delivered charge or electrical efficiency, as function of time for specific experimental conditions. This may facilitate the selection of optimal stimulation parameters. An appropriate estimation of the voltage drop on the tissue or the delivered charge is essential in the effort to understand the neuro-electric interface. At the same time a correct characterization of electrode impedance is important for a better electrode design. For the same applied current the electrical efficiency is little higher for monopolar configuration in respect with the values for bipolar configuration.

REFERENCES

de Boer R.W., van Osteroom A., *Electrical Properties of Platinum Electrodes: Impedance Measurements and Time-Domain Analysis*, Med. Biol. Eng. Comput., **16**, 1-10 (1978).

Coffey R.J., *Deep Brain Stimulation Devices: A Brief Technical History and Review*, Artificial Organs, **33**, 208-220 (2008).

Franks W., Schenker I., Schmutz P., *Impedance Characterization and Modeling of Electrodes for Biomedical Applications*, IEEE Trans. Biomed. Eng., **52**, 1295-1302 (2005).

Hariz M., Blomstedt P., Zrinzo L., *Future of Brain Stimulation: New Targets, New Indications, New Technology*, Mov Disord., **28**, *13*, 1784-1792 (2013).

Geddes L.A., *Historical Evolution of Circuit Models for the Electrode-Electrolyte Interface*, Annals of Biomedical Engineering, **25**, 1-14 (1997).

Haueisen J., Ramon C., Eiselt M., Brauer H., Nowak H., *Influence of Tissue Resistivities on Neuromagnetic Fields and Electric Potentials Studied with a Finite Element Model of the Head*, IEEE Trans. Biomed. Eng., **44**, *8*, 727-732 (1997).

Holsheimer J., Dijkstra E.A., Demeulemeester H., Nuttin B., *Chronaxie Calculated from Current–Duration and Voltage–Duration Data*, J. Neurosci. Method, **97**, 45-50 (2009).

Lempka S.F., Miocinovic S., Johnson M.D., Vitek J.L., McIntyre C.C., *In Vivo Impedance Spectroscopy of Deep Brain Stimulation Electrodes*, J. Neural Eng., **6**, 321-332 (2009).

Lilly J.C., In: Sheer D.E. (Ed.), *Electrical Stimulation of the Brain. An Interdisciplinary Survey of Neurobehavioral Integrative Systems*, Austin, TX: University of Texas Press, 60-64 (1961).

Miocinovic S., Somayajula S., Chitnis S., Vitek J.L., *History, Applications, and Mechanisms of Deep Brain Stimulation*, JAMA Neurol., **70**, *2*, 163-171 (2013).

Morgan H., Sun T., Holmes D., Gawad S., Green N.G., *Single Cell Dielectric Spectroscopy*, J. Phys. D 40, 61-68 (2007).

Neagu B., Neagu E., *Impedance Characterization of a Deep Brain Stimulating Electrode: AC Electrochemical Impedance Spectroscopy*, Bul. Inst. Polit. Iaşi, s. Mat., Mec. Teor., Fiz., **62(66)**, *3*, 37-50 (2016).

Rattay F., *Analysis of Models for Extracellular Fiber Stimulation*, IEEE Trans. Biomed. Eng., **36**, 676-682 (1989).

Schwan H.P., *Electrode Polarization Impedance and Measurements in Biological Materials*, Ann. N Y Acad. Sci., **148**, *1*, 191-209 (1968).

Shah R.S., Chang S.Y., Min H.K., Cho Z.H., Blaha C.D., Lee K.H., *Deep Brain Stimulation: Technology at the Cutting Edge*, J. Clin. Neurol., **6**, *4*, 167-182 (2010).

Vinter E., Petersen S., Gimsa J., van Rienen U., *Impedance Spectroscopy and Cell Constant of the Electrodes for Deep Brain Stimulation*, Excerpt from the Proceedings of the COMSOL Conference Milan 2009, 282-286.

Walckiers G., Fuchs B., Thiran J.P., Mosig J.R., Pollo C., *Influence of the Implanted Pulse Generator as Reference Electrode in Finite Element Model of Monopolar Deep Brain Stimulation*, J. Neurosci. Methods, **186**, 90-96 (2010).

Wei X.F., Grill W.M., *Impedance Characteristics of Deep Brain Stimulation Electrodes in Vitro and in Vivo*, J. Neural Eng., **6**, 89-98 (2009).
Weinman J., Mahler J., *An Analysis of Electrical Properties of Metal Electrodes*, Med. Electron. Biol. Engng., **2**, 299-310 (2010).

CARACTERIZAREA IMPEDANŢEI ELECTRODULUI PENTRU STIMULARE PROFUNDĂ ÎN CREIER: RĂSPUNSUL TRANZITORIU LA IMPULS

(Rezumat)

Scopul lucrării este de a prezenta o ecuaţie pentru impedanţa instantanee $Z(t)$ a electrodului pentru cazul când este folosit cu impulsuri de curent similare ca valoare cu acelea folosite pentru aplicaţii clinice. $Z(t)$ creşte cu creşterea timpului t, fiind proporţional cu $t^{0,9}$ şi descreşte cu creşterea tensiunii U, cu creşterea curentului I şi scăderea rezistivităţii ρ. Propunem o ecuaţie pentru $Z(t)$ pentru diferite valori ale lui I şi ρ ($Z_{I,\rho}(t)$). Această ecuaţie este folosită pentru a calcula parametrii de interes pentru un anumit pacient, de exemplu, tensiunea necesară pentru a injecta un curent de o anumită valoare, sarcina injectată, randamentul electric al electrodului, etc. ca funcţie de timp pentru condiţii particulare date. Pentru o valoare dată a tensiunii aplicate, sarcina injectată şi randamentul electric sunt puţin mai mari pentru configuraţia monopolară în comparaţie cu valorile pentru configuraţia bipolară, iar diferenţa scade dacă ρ creşte.

BULETINUL INSTITUTULUI POLITEHNIC DIN IAŞI
Publicat de
Universitatea Tehnică „Gheorghe Asachi” din Iaşi
Volumul 62 (66), Numărul 4, 2016
Secţia
MATEMATICĂ. MECANICĂ TEORETICĂ. FIZICĂ

COMPUTATIONAL STUDY OF TWO CARBANION MONO-SUBSTITUTED PYRIDAZINIUM YLIDS

BY

ANTONINA GRITCO-TODIRAȘCU[1], ANA-CEZARINA MOROȘANU[1], LILIANA MIHAELA IVAN[1], CORINA CHEPTEA[2] and DANA ORTANSA DOROHOI[1,*]

[1]“Alexandru Ioan Cuza” University of Iaşi,
Faculty of Physics
[2]“Grigore T. Popa” University of Medicine and Pharmacy, Iaşi,
Faculty of Bioengineering

Received: November 23, 2016
Accepted for publication: December 17, 2016

Abstract. Two carbanion mono-substituted pyridazinium ylids were subjected to a quantum mechanical study based on Spartan’14 programs. Optimized geometry, energetic characteristics, dipole moment, polarizability and other properties were established by three methods offered by Spartan’14. The length of the covalent bonds, the charge distribution near molecular atoms resulted from PM3 method are also given in the article.

Keywords: pyridazinium-p-nitro-phenacylid; (p-phenyl)-p-phenyl-pyridazinium-p-nitro-phenacylid; quantum chemical analysis; Spartan’14.

1. Introduction

Pyridazinium ylids are cycloimmonium ylids having as cation one pyridazinium heterocycle (Zugrăvescu and Petrovanu, 1976; Dorohoi *et al.*, 1994).

[*]Corresponding author; *e-mail*: ddorohoi@uaic.ro

The carbanion mono-substituted ylids possess one hydrogen atom and one atomic group as substituents at their carbanion (Petrovanu *et al*., 1993; Dorohoi and Holban, 1993; Mangalagiu *et al*., 2000). The stability of these ylids increases with the group electronegativity of the substituent attached to the negative carbanion. The carbanion mono-substituted pyridazinium ylids can be used as acid-basic indicators (Zugrăvescu and Petrovanu, 1976), or as precursors in chemical reactions for obtaining new heterocycle compounds (Dorohoi *et al*., 1997/1998; Mangalagiu *et al*., 1999; Dorohoi *et al*., 2002). Recently, they were tested as compounds with pharmacological action (Mantu *et al*., 2010; Mangalagiu *et al*., 1998).

The aim of this paper is to achieve a quantum-chemical study of two carbanion mono-substituted pyridazinium ylids in order to establish the contribution of the heterocycle to the structure and molecular parameters of these ylids.

The studied ylids are:

– Pyridazinium p-nitro-phenacylid (molecule noted P1 – Fig. 1*a*);

– (p-Phenyl) - (p phenyl) - pyridazinium p nitro phenacylid (molecule noted P2 – Fig. 1*b*).

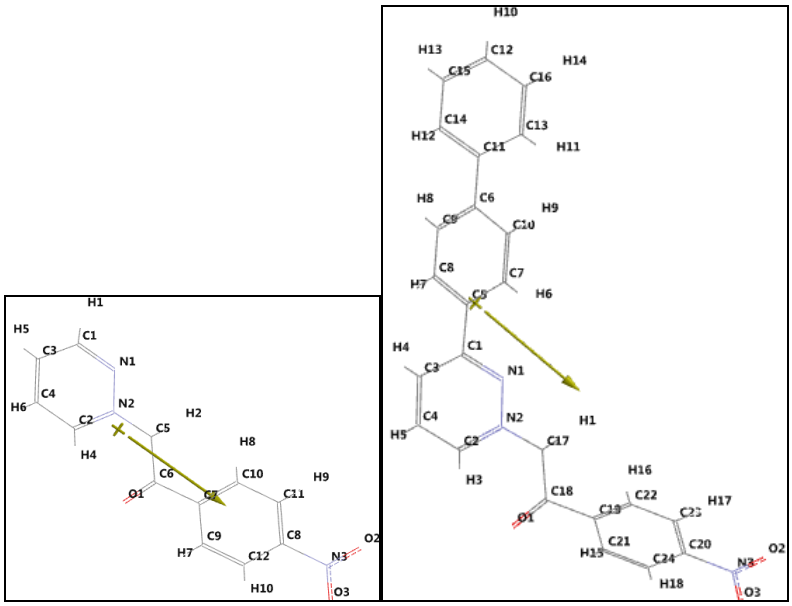

a *b*

Fig. 1 – Skeletal formula and labeled atoms of: (*a*) P1 molecule and (*b*) P2 molecule.

2. Simulation Details

The molecular modeling programs used was Spartan'14 (Spartan'14; Young, 2001). Spartan provides access to several common spectral properties, in particular infrared spectra, Raman spectra, NMR spectra and UV/visible spectra. Spartan provides a variety of graphical tools for interpreting the results of calculations, such as structure models, molecular orbitals, electron and spin densities, local ionization potentials and electrostatic potentials.

Spartan accesses two different databases of information obtained from quantum chemical calculations on stable molecules: Spartan Molecular Database (SMD), containing structures, energies and limited atomic and molecular properties, and Spartan Spectra and Properties Database (SSPD), containing structures, energies and a more extensive selection of atomic and molecular properties.

3. Computational Results

The results of the quantum mechanical calculations performed based on Spartan'14 (Spartan'14) are discussed below.

The optimized geometry given by Spartan'14 is illustrated in Fig. 2*a* and *b* for the two studied ylids. The dipole moment in the ground state of the studied molecules is oriented from the positive part of molecule towards its carbanion (Figs. 2*a* and *b*). From Fig. 2 it results that the ground state dipole moments of the isolated molecules under the study are oriented parallel to the ylid bond (N^+-C^-).

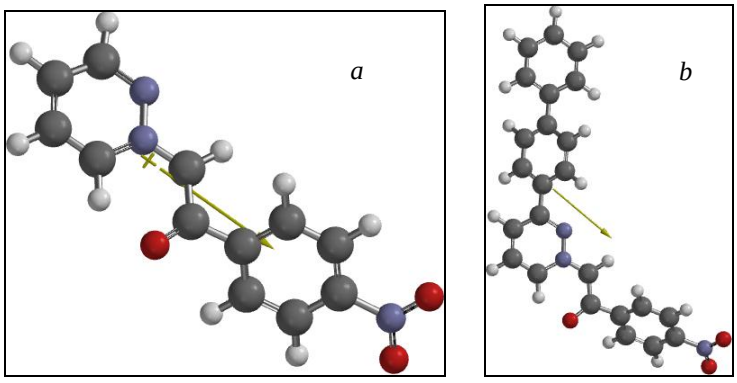

Fig. 2 – The optimized geometry for: (*a*) P1 molecule and (*b*) P2 molecule.

Some molecular parameters obtained in quantum-chemical analysis are listed in Table 1 for P1 molecule and in Table 2 for P2 molecule. The properties of the two molecules were calculated using three different methods offered by Spartan: Semi-empirical Models, Hartree-Fock Models and Density Functional Models.

Semi-empirical Models (Spartan'14) are the simplest methods based on quantum mechanics. They are applicable to molecules containing 100 - 200 atoms. The PM3 model generally provides geometries in good accord with experimental structures. Semi-empirical models are available for the calculation of IR spectra but do not provide a very good account. They are not available for the calculation of Raman, NMR or UV/visible spectra.

Hartree-Fock models (Spartan'14) result from the Schrödinger equation, by requiring that the electrons be independent particles. The motions of electrons in molecules (molecular orbitals) are approximated by a sum of the motions of electrons in atoms (atomic orbitals). Hartree-Fock models permit the calculation of IR, Raman, NMR and UV/visible spectra.

Models that eliminate or reduce the Hartree-Fock approximation are named correlated models (Spartan'14). These divide into two broad categories: density functional models and wave function-based models. Density functional models explicitly introduce an approximate ("empirical") correlation term (a functional). They are not much costlier in terms of computation time than Hartree-Fock models. Density functional models provide an excellent account of the equilibrium geometries of organic molecules. Density functional models are available for the calculation of IR, Raman, NMR and UV/visible spectra.

Table 1
Molecular Properties of P1, Using Spartan'14 Program

Molecular properties	Semi-empirical PM3 Method	Hartree-Fock Method	Density Functional Method
Molecule			
Weight	243.222 amu	243.222 amu	243.222 amu
Energy	225.94 kJ/mol	-842.606588 au	-851.917629 au
Energy (aq)	196.15 kJ/mol	-842.615526 au	-851.925733 au
Solvation E	-29.79 kJ/mol	-23.47 kJ/mol	-21.28 kJ/mol
Dipole Moment	7.55 debye	11.02 debye	8.90 debye
E HOMO	-8.81 eV	-7.59 eV	-5.63 eV
E LUMO	-1.47 eV	0.55 eV	-2.78 eV
Tautomers	0	0	0
Conformers	4	4	4
QSAR			
Area	254.59 $Å^2$	248.62 $Å^2$	250.54 $Å^2$
Volume	232.99 $Å^3$	229.62 $Å^3$	231.09 $Å^3$
PSA	61.719 $Å^2$	60.440 $Å^2$	60.672 $Å^2$
Ovality	1.39	1.37	1.38
Polarizability	58.54	58.08	59.45
HBD Count	0	0	0
HBA Count	6	6	6
Temperature	298.15 K	298.15 K	298.15 K

Some information such as area, volume, weight, numbers of tautomers and conformers, ovality, polarizability, hydrogen bond donor and hydrogen bond acceptor counts have appropriate values in the three methods (PM3, Hartree-Fock and Density Functional Method). The values obtained for energetic parameters in the three methods from Spartan '14 are different. The differences are probably due to the approximations regarding the electron motions in molecule. Comparing the data from Tables 1 and 2, some difference between the parameters computed for the two studied ylids (in their gaseous phase) are evident:

– The energetic values are higher for P2 than P1.

– Area, volume, ovality are higher for P2 compared with P1.

– The dipole moment and polarizability of P2 are also higher than P1.

– The two molecules have the same number of tautomers, conformers, HBD and HBA counts.

– The values of frontier HOMO and LUMO computed by semi empirical PM3 and Hartree-Fock methods are appropriate for the two studied ylids, while they substantially differ from those computed by Density Functional Method.

Table 2

Molecular Properties of P2, Using Spartan'14 Program

Molecular properties	Semi-empirical PM3 Method	Hartree-Fock Method	Density Functional Method
Molecule			
Weight	395.418 amu	395.418 amu	395.418 amu
Energy	435.85 kJ/mol	-1299.15001 au	-1313.67030 au
Energy (aq)	402.60 kJ/mol	-1299.15880 au	-1313.67915 au
Solvation E	-33.25 kJ/mol	-23.08 kJ/mol	-23.24 kJ/mol
Dipole Moment	8.28 debye	12.00 debye	10.06 debye
E HOMO	-8.72 eV	-7.50 eV	-5.50 eV
E LUMO	-1.40 eV	0.64 eV	-2.69 eV
Tautomers	0	0	0
Conformers	4	4	4
QSAR			
Area	408.28 $Å^2$	415.79 $Å^2$	410.05 $Å^2$
Volume	395.27 $Å^3$	399.88 $Å^3$	397.66 $Å^3$
PSA	59.517 $Å^2$	61.338 $Å^2$	59.697 $Å^2$
Ovality	1.57	1.58	1.57
Polarizability	71.52	72.09	72.97
HBD Count	0	0	0
HBA Count	6	6	6
Temperature	298.15 K	298.15 K	298.15 K

Electrostatic charges for the two molecules, calculated by PM3 from Spartan program, are shown in Fig. 3*a* and *b*.

Appropriate values for the charges near the atoms of the ylid bond (N^+-C^-) are given by PM3 from Spartan '14 programs.

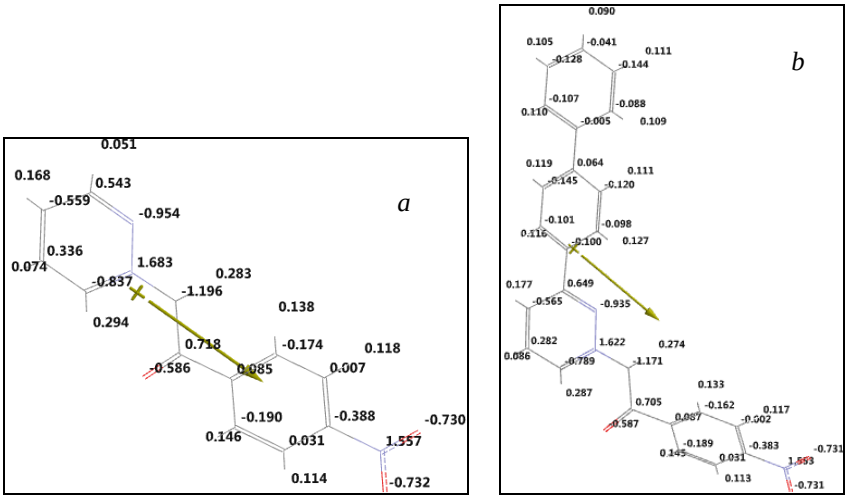

Fig. 3 – Electrostatic Charge for: (*a*) P1 molecule and (*b*) P2 molecule.

Spartan program can evaluate the lengths of chemical bonds between atoms of the molecule, angles between these bonds and dihedral angles. In Table 3 there are shown the lengths of chemical bonds for P1 molecule. Table 4 shows, for example, the values calculated by Spartan for some angles between chemical bonds and respectively dihedral angles. The atoms of P1 molecule are labeled in Fig. 1.

Table 3

Lengths of Chemical Bonds for P1 Molecule

Chemical bond	Bond length (Å)	Chemical bond	Bond length (Å)	Chemical bond	Bond length (Å)	Chemical bond	Bond length (Å)
C1-C3	1.393	C3-H5	1.094	C6-C7	1.495	C9-H7	1.097
C3=C4	1.395	C4-H6	1.095	C7-C9	1.395	C12-H10	1.099
C4-C2	1.384	C2-H4	1.121	C9=C12	1.390	C11-H9	1.099
C2=N2	1.395	N2-C5	1.356	C12-C8	1.399	C10-H8	1.097
N2-N1	1.356	C5-H2	1.100	C8=C11	1.400	C8-N3	1.498
N1=C1	1.353	C5-C6	1.452	C11-C10	1.389	N3=O2	1.215
C1-H1	1.096	C6=O1	1.230	C10=C7	1.395	N3=O3	1.215

Table 4
The Measure of Some Angles and Dihedrals for P1 Molecule

Angle/dihedral	Measure
Angle (C10, C11, C8)	119.92°
Angle (C8, N3, O2)	119.42°
Angle (O2, N3, O3)	121.14°
Dihedral (C5, C6, C7, C10)	52.83°
Dihedral (C11, C8, N3, O2)	1.45°
Dihedral (N2, C5, C6, O1)	-0.36°
Dihedral (C2, N2, C5, C6)	0.31°
Dihedral (C5, C6, C7, C10)	52.83°
Dihedral (O1,C6,C7,C9)	52.17°
Dihedral (N1, N2, C5, H2)	-0.34°

As it results from Table 4, in the case of P1 molecule, the dihedral angles (N2, C5, C6, O1), (C2, N2, C5, C6) and (N1, N2, C5, H2) have values near zero degree (-0.36; 0.31 and -0.34, respectively) and, one can assume with enough precision that the covalent bonds C6O1, C5C6 and C5H2 belong to the heterocycle plane. On the other hand, the values of the value of the dihedral angles: (O1, C6, C7, C9) and (C5, C6, C7, C10) are near 52 degrees, indicating a rotation of about 52 degrees of the p-nitro-benzoyl plane relative to the pyridazine plane.

The values of the angles between the covalent bonds (C8, N3, O2) and (O2, N3, O3) and also the dihedral angle (C11, C8, N3, O2) from Table 4 indicate the co planarity of the benzoyl ring and the nitro group substituted in p- position.

Table 5
Lengths of Chemical Bonds for P2 Molecule

Chemical bond	Bond length (Å)	Chemical bond	Bond length (Å)	Chemical bond	Bond length (Å)	Chemical bond	Bond length (Å)
C1-C3	1.401	C6=C9	1.398	C14=C11	1.397	C24-C20	1.400
C3=C4	1.393	C9-C8	1.388	C13-H11	1.096	C20=C23	1.400
C4-C2	1.384	C8-C5	1.399	C14-H12	1.096	C23-C22	1.389
C2=N2	1.394	C7-H6	1.096	C15-H13	1.095	C22=C19	1.395
N2-N1	1.351	C8-H7	1.097	C16-H14	1.095	C22-H16	1.097
N1=C1	1.365	C9-H8	1.096	C12-H10	1.095	C21-H15	1.097
C3-H4	1.095	C10-H9	1.097	N2-C17	1.358	C23-H17	1.099
C4-H5	1.095	C6-C11	1.469	C17-H1	1.100	C24-H18	1.100
C2-H3	1.121	C11-C13	1.397	C17-C18	1.451	C20-N3	1.498
C1-C5	1.470	C13=C16	1.390	C18=O1	1.230	N3-O2	1.216
C5-C7	1.397	C16-C12	1.391	C18-C19	1.496	N3-O3	1.215
C7=C10	1.390	C12=C15	1.391	C19-C21	1.395		
C10-C6	1.397	C15-C14	1.390	C21=C24	1.390		

The lengths of the chemical bonds and some of important angles and dihedral angles for the spatial orientation of the molecular skeleton of P2 molecule are given in Tables 5 and 6.

By comparing the data of Tables 3 and 5, it results appropriate values (1.356A in P1 and 1.358 in P2) for the length of the ylid bonds: (N_2^+-C^-_5) and (N_2^+-C_{17}^-). They are not influenced by the heterocycle substitution.

The dihedral angles: (N1, N2, C17, H1), (C2, N2, C17, C18) and (N2, C17, C18, O1) having values of about -0.46, 0.41 and -0.21 degrees, respectively, demonstrate that the ylid bond (N_2^+-C_{17}^-) and the covalent bonds C17H1 and C18O1 lye in the heterocycle plane. The values of the dihedral angles (C17, C18, C19, C22) and (O1, C18, C19, C21) near 52 degrees, indicate a rotation of the p-nitro-benzoyl cycle with this degree around the ylid bond. The angles (C20, N3, O2) and (O2, N3, O3), appropriate to 120 degrees (Table 6) demonstrate the sp^2 hybridization of nitrogen atom in nitro group. The dihedral angle (C23, C20, N3, O2) measures about 4 degrees; it demonstrates a small rotation of the nitro group, relative to the benzoyl ring.

The substituent of the phenyl to the pyridazinium heterocycle in p-position does not modify the relative position of the ylid carbanion to the pyridazinium cycle. This position is similar in both ylids P1 and P2.

Table 6

The Measure of Some Angles and Dihedrals for P2 Molecule

Angle/dihedral	Measure
Angle (C22, C23, C20)	119.92°
Angle (C20, N3, O2)	119.42°
Angle (O2, N3, O3)	121.11°
Dihedral (C17, C18, C19, C22)	52.93°
Dihedral (C23, C20, N3, O2)	-3.83°
Dihedral (N1, N2, C17, H1)	-0.46°
Dihedral (C2, N2, C17, C18)	0.41°
Dihedral (N2, C17, C18, O1)	-0.21°
Dihedral (O1, C18, C19, C21)	52.00°
Dihedral (H7, C8, C5, C1)	-0.76°
Dihedral (N1, C1, C5, C7)	-40.41°
Dihedral (C9, C6, C11, C14)	47.37°
Dihedral (C10, C6, C11, C13)	47.30°
Dihedral (N1, C1, C11, C13)	6.86°

The values of the dihedral angles (H7, C8, C5, C1), (N1, C1, C5, C7), (C9, C6, C11, C14) and (C10, C6, C11, C13) of about -0.76, -40.41, 47.37 and 47.30, respectively, demonstrates that the first benzene cycle substituted in p-position of pyridazinium ring. In the first benzene cycle from the pyridazine ring makes 40.41 degrees with the heterocycle. It results a reduced conjugation

between the heterocycle and this cycle. The angle between the second benzene cycle and the pyridazine ring is of about 6.86^0. Between the two benzene cycles there is an angle of about 47.37^0 as it results from Spartan'14 programs. This relative orientation of the molecular cycles in P2 explains the similitude in the carbanion orientation and in the HOMO and LUMO orbital in two studied ylids.

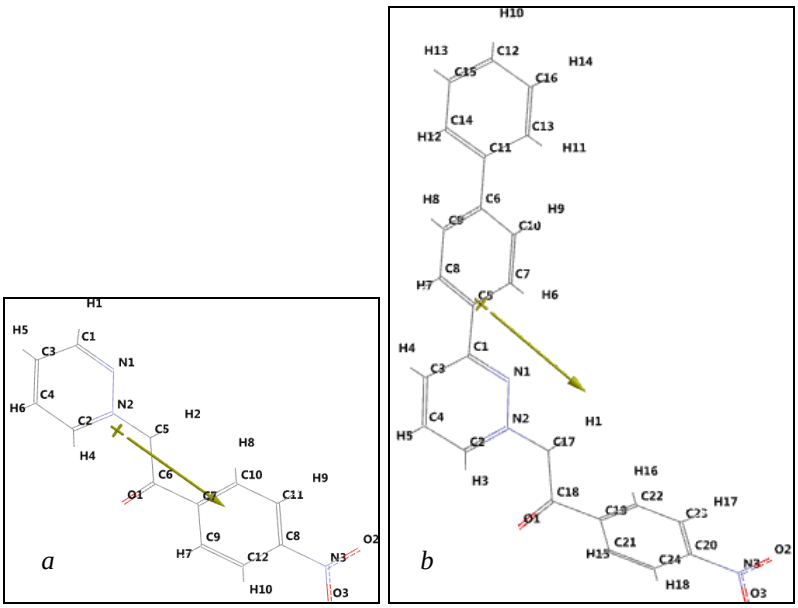

Fig. 4 – The labeled atoms of P1 (*a*) and P2 (*b*) molecules.

Spartan allows graphical display of the HOMO (highest-occupied molecular orbital) and LUMO (lowest-occupied molecular orbital) among other molecular orbitals, the electron density, and the spin density for molecules with unpaired electrons, the electrostatic potential, and the local ionization potential. The highest-energy occupied orbital (the HOMO) is most commonly assumed to be the relevant electron-donor orbital and the lowest-energy unoccupied orbital (the LUMO) is most commonly assumed to be the relevant electron-acceptor orbital. HOMO and LUMO orbitals are shown in Fig. 5 for P1 molecule and in Fig. 6 for P2 molecule, respectively.

By comparing the corresponding HOMO and LUMO in Figs. 5 and 6 it results that the distribution of electron-acceptor and electron-donor orbital in pyridazine heterocycle and in carbanion are alike for the two molecules. The substituent (p-phenyl-p-phenyl) is not affected by ylid bond in P2.

The concentration of electrons may be determined using X-ray diffraction. The highest concentrations are immediately surrounding the atoms. The electron density is a surface that contains most (>99%) of a molecule's

electrons and that roughly corresponds to a space-filling model, that is, a van der Waals surface.

The electrostatic potential map paints the value of the electrostatic potential onto an electron density surface. By convention, colors toward red depict negative potential, while colors toward blue depict positive potential, and colors in between (orange, yellow, and green) depict intermediate values of the potential.

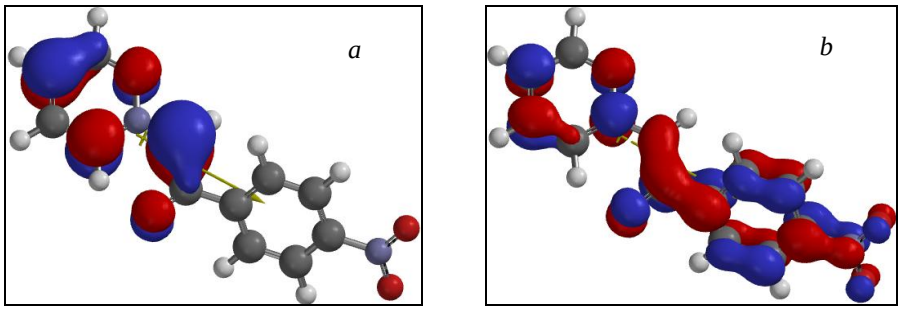

Fig. 5 – (*a*) HOMO and *(b*) LUMO surfaces for P1 molecule.

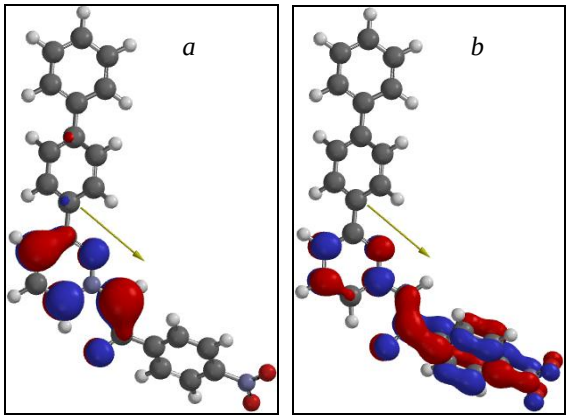

Fig. 6 – (*a*) HOMO and (*b*) LUMO surfaces for P2 molecule.

The local ionization potential map paints the value of the local ionization potential onto an electron density surface. By convention, colors toward red indicate low ionization potential, while colors toward blue indicate high ionization potential.

The LUMO map paints the absolute value of the lowest-unoccupied molecular orbital (the LUMO) onto an electron density surface. By convention, colors near blue indicate high concentration of the LUMO, while colors near red indicate low concentration. A LUMO map indicates where nucleophilic attack

would likely occur. These surfaces are illustrated in Fig. 7 for P1 molecule and Fig. 8 for P2 molecule.

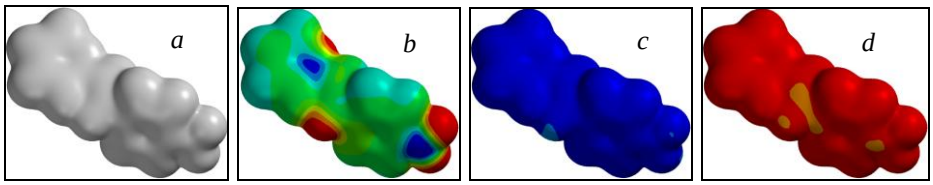

Fig. 7 – (*a*) Density surface, (*b*) electrostatic potential map, (*c*) local ionization potential map and (*d*) |LUMO| map for P1 molecule.

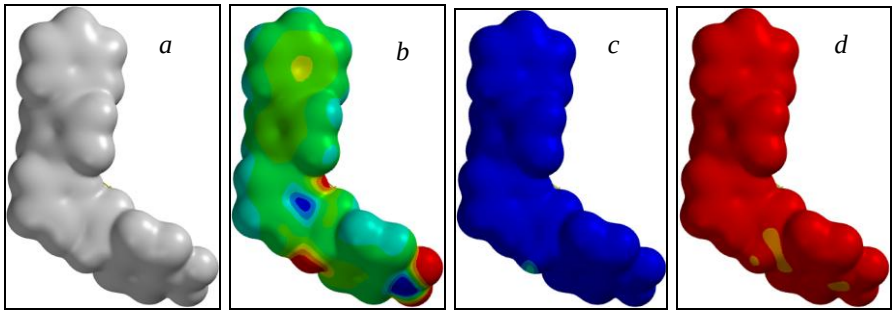

Fig. 8 – (*a*) Density surface, (*b*) electrostatic potential map, (*c*) local ionization potential map and (*d*) |LUMO| map for P2 molecule.

3. Conclusions

The three methods implemented in Spartan'14 give different values for energetic and electro-optical parameters of the two studied pyridazinium ylids, but indicate similar representation of HOMO and LUMO orbital's, of the density surface electrostatic potential map and of the local ionization potential.

The p-Phenyl-(p-phenyl) substituent to the pyridazine ring in P2 molecule is not affected by the ylid carbanion, due to the reduced conjugation between them.

The length and the charge distribution on the ylid bond is not affected by the p-substitution at heterocycle.

REFERENCES

Dorohoi D., Holban V., *Intermolecular Interactions in Some Pyridazinium Ylids Solution*s, J. Mol. Struct., **293**, 1333-136 (1993).

Dorohoi D., Partenie D.H., Anton C., Chiran L., *About the Electronic Absorption Spectra (EAS) and Electronic Diffusion Spectra (EDS) of Some Pyridazinium Ylids*, J. Chim.-Phys, Phys.-Chim. Biol., **91**, *4*, 419-431 (1994).

Dorohoi D., Melnig V., Mangalagiu I., Verdeș D., Delibas I., *Spectral Study of 3+3 Thermal Dimerisation of Carbanion Monosubstituted Pyridazinium Ylides*, Analele Științifice ale Universității "Al. I. Cuza" din Iași, Chimie, **XLIII-XLIV** (sf), 67-72 (1997/1998).

Dorohoi D., Cotleț M., Mangalagiu I., *Spectral Kinetics of 3+3 Dipolar Thermal Dimerization in Some Carbion Mono-Substituted 3-(p-Halo-Phenyl)-Pyridazinium Ylid Solutions*, Int. J. Chem. Kin., **34**, *11*, 613-619 (2002).

Mangalagiu I., Ungureanu M., Mangalagiu G., Grosu G., Petrovanu M., *Antimicrobial Activity of Some Pyrimidinium Compounds*, Ann. Pharm. Fr., **56**, *4*, 181-183 (1998).

Mangalagiu I.I., Olariu R., Caprosu M., Dorohoi D., Cotleț M., Petrovanu M., *Spectral Properties of Some 3-R1-Pyridazinium-P-R2-Phenacylids*, Analele Știintifice ale Universității "Al. I. Cuza" din Iași, Chimie, 7 (s2c) 313-320 (1999).

Mangalagiu I.I., Ungureanu M., Grosu G., Petrov M., *New Pyridazinium Ylids with Antimicrobial Activity*, An. Șt. Univ. Al. I. Cuza, din Iași, s. Chimie, **8** (s2c), 131-134 (2000).

Mantu D., Luca M.C., Moldoveanu C., Zvancioc Ghe., Mangalagiu I.I., *Synthesis and Antituberculosis Activity of Some New Pyridazine Derivatives*, Part II, Eur. J. Med. Chem., **45**, 5164-5168 (2010).

Petrovanu M., Anton C., Dorohoi D.O., Caprosu M., Fulger I., *Visible Absorption Electronic Spectra of Some Pyridazinium Ylides*, Rev. Roum. Chim., **38**, *7*, 759-766 (1993).

Spartan'14 for Windows, Macintosh and Linux, *Tutorial and User's Guide*, January 10, 2014, Wave function, Inc.18401 Von Karman Avenue, Suite 370 Irvine, CA 92612 U.S.A.

Young D., *Computational Chemistry*, Wiley-Interscience, 2001, Appendix A. A.1.6, p. 330, Spartan.

Zugrăvescu I., Petrovanu M., N Ylid Chemistry, McGraw-Hill, New York, 1976.

STUDIUL COMPUTAȚIONAL A DOUĂ PIRIDAZINIUM ILIDE CARBANION MONO-SUBSTITUITE

(Rezumat)

Două pyridazinium ilide carbanion mono-substituite au fost supuse unui studiu cuanto-mechanic utilizând programele din Sparta'14. A fost stabilită distribuția spațială a atomilor în geometria optimizată a celor două molecule. Trei metode oferite de Spartan'14 au fost utilizate pentru a stabili caracteristicile energetice și electro-optice ale celor două molecule. Lungimile legăturilor covalente, orientarea lor spațială dată de valorile unghiurilor dintre legături și a unghiurilor diedre și distribuția de sarcină din vecinătatea atomilor moleculari sunt de asemenea date în acest articol.

BULETINUL INSTITUTULUI POLITEHNIC DIN IAŞI
Publicat de
Universitatea Tehnică „Gheorghe Asachi” din Iaşi
Volumul 62 (66), Numărul 4, 2016
Secţia
MATEMATICĂ. MECANICĂ TEORETICĂ. FIZICĂ

ANALITICAL AND PHYSICAL MODELING OF THE NAVAL MAGNETIC SIGNATURE

BY

OCTAVIAN BALTAG[1] and GEORGIANA ROȘU[2,*]

[1]“Alexandru Ioan Cuza” University of Iași,
Faculty of Physics
[2]Military Technical Academy of Bucharest

Received: November 5, 2016
Accepted for publication: December 15, 2016

Abstract. The paper presents the theoretical and experimental results regarding one of the ship’s physical fields: the magnetic signature and its interaction with the Earth’s magnetic field. The analytical modeling is based on a simplified model, valid at a certain distance from the ship hull, determined by the ship’s own disruptive field value and its temporal evolution caused by ship dynamics in the marine environment. The national theoretical and experimental research stage is presented, and compared to international research. There is described the simplified ellipsoidal shell model, and magnetic signature of an ellipsoidal ferromagnetic layer is computed. The theoretical results are compared to the measurements performed on a real ship modeled through the ellipsoidal shell, and the physical model of the same ship, obtained by applying similarity criteria. There is noticed a good correlation and concordance among magnetic field results obtained through theoretical and experimental models and real ship measurements.

Keywords: ship magnetism; deperming; degaussing.

[*]Corresponding author; *e-mail*: georgianamarin01@gmail.com

1. Introduction

The naval magnetic signature represents the ship's magnetic field distribution in the underwater environment, characterized by uniqueness and developed mainly by the Earth's magnetic field acting upon the ship's ferromagnetic hull. The ship magnetization can be produced during its construction and also during its exploitation.

The ship magnetization during construction is called permanent magnetization, has relatively constant value, without reaching the saturation of the ferromagnetic masses, is stable in time, and is characteristic to each type of ship. The ship magnetization during exploitation is called induced magnetization, having a variable character, with the magnitude and direction depending also on the ship type.

The permanent magnetism depends upon:

– the ratio between the ship's main dimensions;

– the ship's secondary ferromagnetic masses – their shape, placement, and ferromagnetic properties;

– the ship berth orientation and the geographic latitude of the naval shipyard;

– the ship construction technology.

The induced magnetism depends upon:

– the ratio between the ship's main dimensions: length, width, draft;

– the geographic latitude of the ship position;

– the ship's heading – its direction relative to the meridian;

– the magnetic properties of the materials used in the ship's hull and its secondary equipment, as well as their distribution along the ship.

Knowing these two fields is important, being connected to danger level to which the ship is exposed during exploitation. For this purpose, the ship is subjected to diagnosis operations in specialized naval ranges, in order to determine the ship's magnetic field components and for applying magnetic signature reduction techniques (Baltag 2003, Holmes 2006).

The research of magnetic signature employs both experimental and theoretical methods: experimental techniques for the ship magnetic characterization in magnetic ranges or through physical models, and theoretical methods for modeling and virtual simulation. The magnetic signature modeling initially used simplified analytical models: the dipoles array, magnetic charges, and magnetic moments methods, along with the physical modeling of the ship at a small scale. Common current methods employ dedicated numerical models capable of generating a magnetic signature specific to each type of ship.

Most methods use the finite element technique, due to its flexibility and adaptability to complex geometries of the naval architecture: FEMM, ANSYS, COMSOL, FLUX3D, etc. In order to minimize the surface ships and submarines vulnerability, there have been developed magnetometric techniques

for the control of magnetic fields generated by electromagnetic installations and systems onboard the ship, and for those related to static and dynamic signature characteristic to the ferromagnetic hull ship (Roșu, 2015).

2. The Magnetic Field Mathematical Model

According to the classical approach, the ship magnetic field is stationary, thus Maxwell's equations are reduced to the magnetostatic form (Bansal, 2004):

$$\nabla x\overline{H} = 0 \tag{1}$$

$$\nabla \circ \overline{B} = 0 \tag{2}$$

It is considered that the field sources are located on the hull or inside it, and there are not taken into count the circuits with circulating electric currents.

The model closest to reality and the most convenient representation of the ship, is the ellipsoidal shell model (Aird, 2000), in which the ship is approximated by an ellipsoid body bounded inside and outside by two ellipsoidal surfaces, with the major axis along the ellipsoid's symmetry axis, and minor axis perpendicular to it – as represented in Fig. 1. The ellipsoid is laying in magnetic field oriented at a particular angle to the ship's major axis.

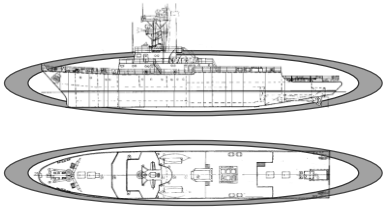

Fig. 1 − The ship representation and its ellipsoidal shell model.

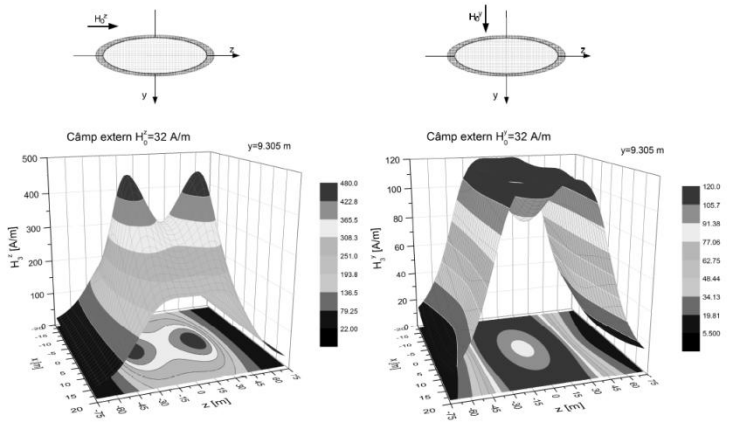

Fig. 2 – The ellipsoidal shell magnetic field distribution, induced by an external field oriented parallel and perpendicular to the ellipsoid's major axis, respectively.

The ship's magnetic field is obtained from the magnetic potential gradient (Roșu, 2015), expressed in ellipsoidal coordinates:

$$\nabla\Phi = \vec{\xi}\frac{1}{c}\sqrt{\frac{\xi^2-1}{\xi^2-\eta^2}}\frac{\partial\Phi}{\partial\xi} + \vec{\eta}\frac{1}{c}\sqrt{\frac{1-\eta^2}{\xi^2-\eta^2}}\frac{\partial\Phi}{\partial\eta} + \vec{\phi}\frac{1}{c}\frac{1}{\sqrt{\left(\xi^2-1\right)\left(1-\eta^2\right)}}\frac{\partial\Phi}{\partial\phi} \quad (3)$$

Fig. 2 describes the magnetic field distribution below the ellipsoidal shell, for an external field of 32 A/m, in two situations. Based on the magnetic field representation, its gradient can be determined. A significantly higher induced magnetic field is obtained for the external field oriented along the major axis of the ellipsoid, as compared to the case of vertical external field, proving that the ellipsoidal geometry tends to magnetize on its major axis.

3. The Physical Scale Model and Magnetic Signature Analysis

Physical scale modeling of ships constitutes a less laborious and less expensive solution for the magnetic characterization of the ship. The study was conducted by respecting the geometrical and physical similarity criteria corrected by factors determined by the magnetic properties of the material used for the simulated ship. There was selected a particular ship for analysis, having the following characteristics: length L = 60 m, width B = 10 m, draft T = 3 m, height D = 5 m. The ship hull is built from high strength naval steel, of 12 mm thickness, relative magnetic permeability μ = 180, and electrical conductivity σ = 4.8 MS/m. The similarity criteria applied to the model refer to geometrical and physical similitude (Kunes, 2012). The geometrical similarity is ensured by following the hull geometry and maintaining constant ratio between the ship and the model main dimensions, according to:

$$\frac{L}{L'} = \frac{B}{B'} = \frac{h_k}{h_k'} = m \quad (4)$$

where h is the depth from the ship keel to the measurement plane, and m denotes the model scaling factor. The two criteria of physical similarity are (Constantinescu, 2010):

$$\Pi_1 = \frac{\sigma_0\mu_0 I_o^2}{T} \quad (5)$$

$$\Pi_2 = \frac{\varepsilon_0}{\sigma_o T} \quad (6)$$

By neglecting the displacement currents, only the first similarity criterion should be ensured. Since the ship's own magnetic field varies slowly in

time, it is considered that the magnetic field variation has the same period T for both ship and model, and therefore neglected.

Practically, there are two scales for modeling the ship: one scale for the main dimensions, and another for the sheet thickness. If the sheet thickness and the magnetic permeability of the physical scale model are denoted by d' and μ', respectively, then their product can be computed through: $d'\mu' = d\mu/m$. The simultaneous fulfillment of two conditions needs to be taken into account, obtained from the first criterion and the condition of proportionality of the thickness and permeability product, thus producing the third similarity criteria:

$$\Pi_3 = \sigma_0 d_0^2 \mu_0^3 \tag{7}$$

This final similarity criterion refers to the proportionality of magnetic properties, main dimensions and sheet thickness of the ship and model, respectively (Roșu, 2014).

4. Comparison of Models to the Real Ship Signature

There was used for comparison a set of magnetic field measurements of the ship for which the scale model was built. The measurements recorded the vertical component of the magnetic signature, below the ship keel, at normal measurement depth, ranging from bow to stern, as represented in Fig. 3. Measurements performed on the vessel Bz_nava were then normalized to be compared with the vertical component values Bz_model, registered under the model keel. The scaling factor used for the ship model 1:100, was also employed for scaling the measurement depth.

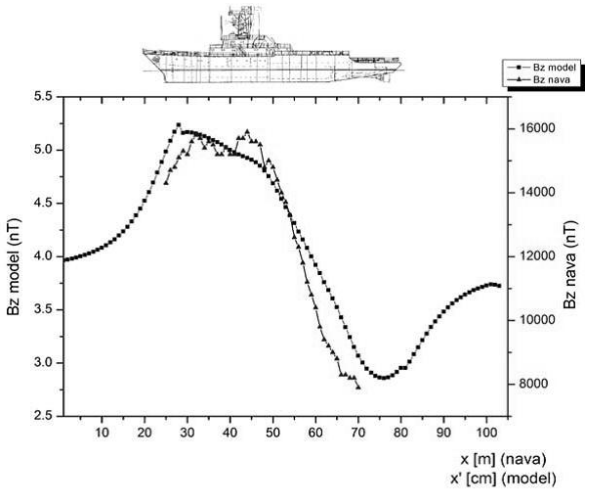

Fig. 3 – The magnetic signature vertical component of the model and the ship, respectively.

There is noticed a high correlation between the values of the vertical magnetic signature of the physical model and that of the ship. Differences can be explained by the presence of installations and equipment generating magnetic field onboard the ship, which was not reproduced in the scale model.

Table 1
Comparison Between the Analytical Model Results - Signature Measurements

Quantity	Ellipsoidal shell model	Real ship
Main dimensions	length: $2a_0$ = 74.4 m width: $2b_0$ = 12.4 m semi-height: b_0 = 6.2 m	L = 60 m, Width: l = 10 m T = 3 m, Depth: D = 5 m
Measurement / Computation depth	$h_{computed}$ = 6.2 m below ellipsoidal shell	$h_{measure}$ = 7 m below ship keel
External field	Vertical field 32 A/m ≈ 400 mOe (Fig. 2 and Fig. 4)	Total geomagnetic field, with dominant vertical component 32 A/m ≈ 400 mOe
Measured / computed values	Total magnetic field	vertical component of the geomagnetic field (40000 nT), plus the ship permanent and induced magnetization
Field values range (external field included)	5.5 A/m … 120 A/m	42,435 nT … 50,439 nT

In Table 1 there are shown for comparative purposes the analytically computed and the measured field values, below the longitudinal axis of the model, and the ship, respectively, at the specified depths.

5. Conclusions

This paper describes the theoretical and experimental research of the naval magnetic signature, performed by using an ellipsoidal shell model and a physical scale model of a particular ship. For the theoretical model of an ellipsoidal shell, there is computed the magnetization induced by an external field oriented parallel with and perpendicular to the main axis of the chosen ellipsoid, thus revealing the dominant effect of the field component oriented parallel to principal axis of the ellipsoid. For the experimental research, a physical model was built to a scale of 1:100, respecting the proportionality between the main dimensions. The data sets measured for both the actual ship and the physical model, presented different orders of magnitude, but in terms of shape, there appeared a high correlation between the two sets of measurements.

REFERENCES

Aird G.J.C., *Modelling the Induced Magnetic Signature of Naval Vessels*, Ph.D. Thesis, University of Glasgow, Glasgow, 2000.

Baltag O., *Magnetometrie – Aplicații în Mediul Marin*, Performantica, Iași, 2003.

Bansal R., *Handbook of Engineering Electromagnetics*, Marcel Dekker, New York, 2004.

Constantinescu M., *Amprenta magnetică a navei*, Ed. Academiei Navale „Mircea cel Bătrân", Constanța, 2010.

Holmes J.J., *Exploitation of a Ship`s Magnetic Field Signatures*, Morgan & Claypool, San Rafael, 2006.

Kunes I., *Similarity and Modelling in Science and Engineering*, Springer, Cambridge International Publishing, 2012.

Roșu G., *Contribuţii privind modelarea şi reducerea amprentei magnetice la nave*, Teză doctorat, Academia Tehnică Militară, București, 2014.

Roșu G., *Elaborarea, analiza si exploatarea modelelor de amprentă magnetică navală*, Performantica, Iași, 2015.

MODELAREA ANALITICĂ ŞI FIZICĂ A AMPRENTEI MAGNETICE NAVALE

(Rezumat)

Lucrarea prezintă rezultatele unui studiu teoretic și experimental privind unul din câmpurile fizice specifice navelor: câmpul magnetic al navei și interacțiunea navei cu câmpul magnetic terestru. În modelarea analitică se folosește un model simplificat, valabil la o distanță de interes față de corpul navei, interes determinat de valoarea câmpului propriu perturbator și evoluția sa temporală determinată de dinamica navei în mediul acvatic. Se prezintă stadiul cercetărilor teoretice și experimentale în plan intern, comparativ cu cele mondiale. Se prezintă modelul de înveliș elipsoidal simplificat al navei și se calculează amprenta magnetică pentru un model de strat feromagnetic elipsoidal. Se constată o bună corelare și concordanța rezultatelor obținute prin modelarea teoretică, experimentală și cele măsurate pe nava reală.

BULETINUL INSTITUTULUI POLITEHNIC DIN IAŞI
Publicat de
Universitatea Tehnică „Gheorghe Asachi” din Iaşi
Volumul 62 (66), Numărul 4, 2016
Secţia
MATEMATICĂ. MECANICĂ TEORETICĂ. FIZICĂ

PARAMETERS CONTROL OF SOME SPIN VALVE GMR SENSORS WITH SYNTHETIC ANTIFERROMAGNETS

BY

DANIELA IONESCU[1,*] and GABRIELA APREOTESEI[2]

“Gheorghe Asachi” Technical University of Iaşi,
[1]Department of Telecommunications
[2] Department of Physics

Received: November 6, 2016
Accepted for publication: December 14, 2016

Abstract. A simulational analysis of a category of synthetic antiferromagnets (SAF) used in the spin valves for giant magnetoresistance (GMR) sensors was performed. Different structures of the stack of layers in the spin valve were considered in order to improve the strongly antiferromagnetic coupling between a pinned layer and a reference layer (Co hard magnetic alloys), across the spacer layer (Ru, Ta, Ti). Parametrical representations of the resistance-area product variation, ΔRA, and also of the areal storage density were given on graphs, using theoretical considerations and 3D structural simulations performed with the HFSS program. Internal phenomena were considered and also the influence of the external fields. A controlled structure can be obtained, our results indicating a GMR ratio of about 1.3...2.2%, respectively a variation of the resistance-area product of 0.4...16 $m\Omega \cdot \mu m^2$, for an inter-layer thicknesses of 1...1.2 nm, in an applied field of about 2...6 k Oe. Results are dependent of the stack structure, the role on each intermediate exchange layer being essential in the process of performances improving.

Keywords: spin valve; giant magnetoresistence; resistance-area product variation; structural simulation; maxima; parametric analysis.

[*]Corresponding author; *e-mail*: danaity@yahoo.com

1. Introduction

A simulational analysis of a category of synthetic antiferromagnets (SAF) used in the spin valves for GMR sensors was performed in this paper.

Among the applications of the spin-valve structures, electric and electronic devices were manufactured, like: magnetic read heads, magnetic field sensors and GMR (giant magnetoresistance) isolators, microelectromechanical systems (MEMS) and other devices (Hartmann, 2013; Hirota *et al*., 2013). The magnetic field sensors represent a category of interest, being devices used to read data in hard disk drives, or like biosensors, etc.

The layered structures of alternating ferromagnetic and non-magnetic conductive thin films present GMR effect for peculiar sets of materials in contact. If the nature and geometrical parameters of the layers are properly chosen, the quantum mechanical effect can be controlled and performances of the structures are satisfactory for different technical applications. These structures are also used for data storage in the magnetoresistive random-access memories and in the racetrack memories as read heads, as well.

Due to the properties of these material structures, the areal storage densities were increased significantly by using the spin-valve read heads for receiving the information (the bits of data). These read heads replace successfully the thin film inductive heads, and ensure superior performances. In particular, the magnetoresistive ratio, $\Delta R/R$, in the case of layered structures with tunneling effect can reach values of a few percents, having as consequences lower dimensions at device level and high storage density.

2. Characterization of the Spin Valves

Different structures of the stack of layers in the spin valve were considered in order to improve the strongly antiferromagnetic coupling between a pinned and a reference layer, across the spacer layer. Hard magnetic layers based on Co alloys have been analyzed, with a inter-layer of Ru, Ta, Ti and a non-magnetic spacer between the reference and free layers of Cu or alternative.

A parallel sensing current flows in the plan of layers, parallel with the interfaces, in the Current-In-Plane (CIP) geometry. The current density is non-uniform, in layers of different nature but with the same thickness being larger in the layer with lower resistivity (Hartmann, 2013). This is due to the fact that in these cases the free-paths, λ (the average distances along which an electron diffuses between scattering events) are different.

In the considered GMR spin valve, the succession of layers can be described as follows, from above to bottom (Fig. 1):

– the soft magnetic layer (free layer), material: Co_2MnSi, Co_2CuSn, $Co_2FeAl_{0.5}Si_{0.5}$ (Heusler alloys), thickness: 5-10 nm, placed on top, presenting free oriented magnetization;

– the spacer, Cu alloy, + Pt (6-8%) or Ni (13-15%), thickness: 2-4 nm, non-magnetic, with role of exchange decoupler between the magnetic layers;

– the reference layer, material: the same Heusler alloys, thickness: 12 - 25 nm;

– the inter-layer, Ru, Ta, Ti respectively, heavy metal, thickness: 1-2 nm, where intense exchange interactions occurs;

– the hard magnetic layer (pinned layer), the same Heusler alloys, thickness: 20-30 nm, placed on the bottom of the stack, presenting fixed magnetization;

– the substrate, an oxide, MgO (001), NiO, is a pinning layer, antiferromagnetic, fixes the magnetization of the bottom hard magnetic layer and raises its coercivity.

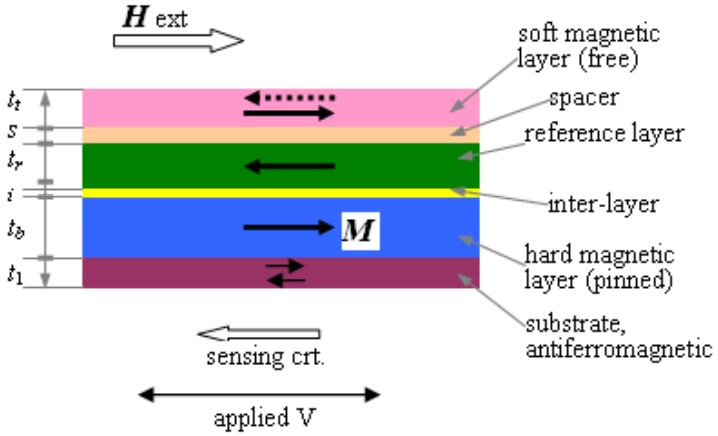

Fig. 1 − The layered structure of the GMR spin valve. The current flows in the layer planes (CIP geometry).

The theoretical support of the oscillatory antiferromagnetic coupling of the magnetic layers in the stack was considered the RKKY (Ruderman-Kittel-Kasuya-Yosida) theory and the quantum well models. The intensity of the antiferromagnetic coupling depends strongly on the nonmagnetic spacer, the dependence being even periodical.

The GMR ratio in the spin valve can be defined as (Hartmann, 2013):

$$\frac{\Delta R}{R_0} = \frac{\Delta R_{\max}}{R_0}\left[\frac{1-\cos\left(\theta_2-\theta_1\right)}{2}\right] \tag{1}$$

where θ_1 and θ_2 are the magnetization orientation angle of the pinned and free FM layers in the spin valve, respectively.

In contrast, the AMR ratio is (Park *et al*., 2011; Tang, 2007):

$$\frac{\Delta\rho}{\rho_0} = \frac{\Delta\rho_{\max}}{\rho_0} \cdot \cos^2\theta \tag{2}$$

where θ = angle between the current and magnetization.

For obtaining the results used for structure optimization, another formula has been applied for estimating the GMR of the considered spin valves, using the sensing current which transforms the change in resistance in a readback voltage, given by simulation:

$$\frac{dR}{R} = \frac{R(H) - R(0)}{R(0)} \tag{3}$$

where $R(H)$ is the resistance of the sample in a magnetic field H, and $R(0)$ is the resistance in null field.

The specific resistance has been computed, AR = the product of the area A through which an assumed uniform CPP current flows and the sample resistance R. The difference between the anti-parallel and parallel states (magnetizations of adjacent ferromagnetic layers in the stack) leads us to the specific resistance variation: $\Delta AR = AR_{anti\parallel} - AR_{\parallel}$.

Considering these formula, the CIP magnetoresistence ratio can be defined as: $MR_{\mathrm{CIP}} = \Delta AR/AR_{\parallel}$, respectively in percents (Yuasa and Djayaprawira, 2007):

$$MR_{\mathrm{CIP}}[\%] = \frac{\Delta AR}{AR_{\parallel}} \tag{4}$$

with the notations used above.

3. Results for the Specific Resistance Variation

A parametrical representation of the resistance-area product variation, ΔRA, was given on graphs, using theoretical considerations and 3D structural simulations performed with the HFSS program. The simulation strategy was conceived considering in the first place the spin valve performances dependence on the properties of the hard magnetic alloy. Internal phenomena were considered and also the influence of the external fields.

A 3D simulational set up was realized in order to reproduce the stack of layers in the spin valve structure, focusing on the spin-orbit coupling modification, induced by geometrical parameters variation under the applied field.

The GMR ratio in function of the spacer layer thickness correlated with the pinned layer thickness was calculated using the formula (3). In the same time, the $\Delta R/R$ evolutions in function of the average grain size in the ferromagnetic layer and the applied magnetic field have been also considered.

Our target was determination of the resistance-area product variation, ΔRA, for the considered read head spin valve in function of spacer thickness *s*, for different inter-layer thicknesses *i*. Results have been represented on the parametrical graphs in Fig. 2.

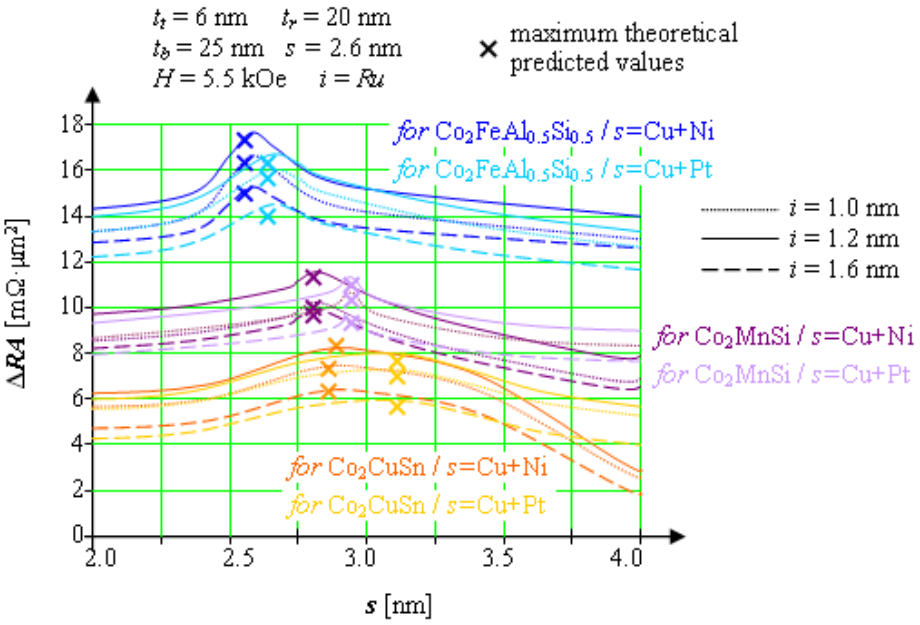

Fig. 2 − Specific resistance variation in function of spacer thickness, for the considered combination of materials in the spin valve GMR sensors. The theoretical predicted values of the ΔRA maximum are indicated on graphs.

One observes a slow increasing and than a decreasing evolution of the ΔRA with s, with a wide maximum, which is more wide and flat then magnetic material magnetization is lower. When the *s* values corresponding to the maximum are transcended, greater the s, weaker the interlayer interactions and weaker the MR. In practice, this effect is more acute due also to the current shunting effects which occur when electrons preferentially flow through the thicker spacer instead of undergoing scattering at the magnetic layer/spacer interfaces (Hartmann, 2013; Covingtona *et al*., 2001).

Specific resistance variation presents a maximum determined by combined effects like the hysteresis phenomenon (the maximum magnitude depends on value of the hysteresis magnetization – field) and the defects at

interfaces level. The pinhole defects degrade significantly the MR due to the direct interactions between the magnetic layers, the effect which is also more acute in practice (Hirota *et al*., 2013).

In order to determine the performances of the considered spin valve GMR sensors, we have determined the variation of the resistance-area product (ΔRA, [mΩ·μm^2]) of read head spin valve in function of spin diffusion length l_{sf}, [nm], which is in our case of tens of nm order for the spin valves with Heusler alloys.

Variation of the resistance-area product (ΔRA, [mΩ·μm^2]) of read head spin valves in function of reference layer thickness [nm] have also been determined considering the intense electron scattering phenomena occurring in this layer and the tunneling effects.

Using and combining the results, we have determined and represented on graphs (Fig. 3) the parametrical evolution of the areal storage density at spin valve level, for a continuous modification of the specific resistance variation, in the case of the considered hard magnetic materials (Heusler alloys) in the spin valve GMR sensors.

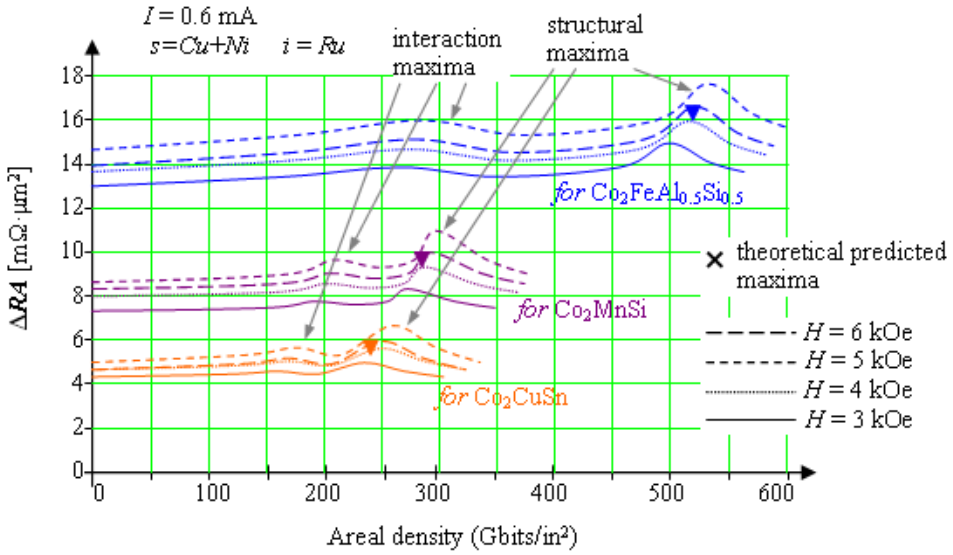

Fig. 3 − Evolution of the areal density for a continuous modification of the specific resistance variation, for the considered hard magnetic materials in the spin valve GMR sensors. Structural, respectively interaction maxima of the ΔRA, present in different domains of the areal density values, are indicated on graphs.

Variations of the resistance-area product ΔRA, [mΩ·μm^2] of a few units are characteristic for the considered hard magnetic materials in the read head spin valve, when the areal density evolves up to 300 Gbit/in^2, respectively 500 Gbit/in^2

for different alloy nature, as we have indicated on graphs. Evolutions for some specific sub-domains present maxima, which can be characterized like structural and interaction maxima.

The main structural maximum of the specific resistance variation, present on each graph, is imposed by the magnetic ion in the hard magnetic alloy of Heusler type. The maximum characteristics depend on the internal interactions in the exchange coupled system, hard - soft magnetic. If the alloy structure changes, the maximum shifts consistently and also its magnitude modifies.

For each type of magnetic material, interaction maxima occurs, generally less intense than the structural maximum. These maxima are present for materials with a common magnetic ion (Co in our case), and are controlled by other factors, like the resonant coupling phenomena between structure, external field H_{ext} and the sensing current I.

The magnitude of the maxima is imposed finally on the spin current, the magnetization dynamics being determined by the torques moving the spins, torques generated by the exchange interaction between conduction electrons and domain wall magnetizations, under the H_{ext} influence. Superior performances of the spin valve GMR sensors can be achieved by correlation of the magnetic material nature and geometrical parameters of the reference layer and inter-layer in the spin valve.

4. Discussions and Conclusions

A controlled structure of the spin valve can be obtained, using the parameters dependence determined by simulation. A lot of parameters characterizing the spin valve structure are implied, like magnetic and non-magnetic materials nature, layer thicknesses, grain sizes in the magnetic alloys, spin diffusion length and defect rates, but not only.

A discussion of the phenomena based on the simulation results can be opened. Among the conclusions, one can formulate the followings.

The maxima of the specific resistance variation, ΔRA, depend on the hysteresis phenomenon inside the magnetic material and at structure level and also by the defects at interface level.

The areal storage density evolves when ΔRA varies in the domain of interest corresponding to the superior values of the MR ratio obtained for the analyzed structures by parameters correlation. Structural and interaction maxima are present on graphs, which are function of the hard magnetic alloy nature and depend on the coupling between substance and field. Phenomenologically speaking, the maxima magnitude is dependent on the spin current flowing in the spin valve layers.

The obtained results have indicated us a GMR ratio of about 1.3...2.2%, respectively a variation of the resistance-area product of 0.4...16 $m\Omega \cdot \mu m^2$, with

maxima in the last third of the scale, for an inter-layer thicknesses of 1...1.2 nm, in an applied field of about 2...6 k Oe. The results are dependent of the stack structure in the spin valve, the role on each intermediate exchange layer being essential in the process of performances improving.

REFERENCES

Covingtona M., Rebei A., Parker G.J., Seigler M.A., *Spin Momentum Transfer in Current Perpendicular to the Plane Spin Valves*, Fujitsu Sci. Tech. J., **37**, *2*, 174-182 (2001).

Hartmann U., *Magnetic Multilayers and Giant Magnetoresistance: Fundamentals and Industrial Applications*, Springer Science & Business Media, 2013.

Hirota E., Sakakima H., Inomata K., *Giant Magneto-Resistance Devices*, Springer Science & Business Media, 2013

Park B.G., Wunderlich J., Martí X., Holý V., Kurosaki Y., Yamada M., Yamamoto H., Nishide A., Hayakawa J., Takahashi H., Shick A.B., Jungwirth T., *A Spin-Valve-Like Magnetoresistance of an Antiferromagnet-Based Tunnel Junction*, Nat. Mater., **10**, *5*, 347-351 (2011).

Tang X., *Magnetotransport and Magnetization Reversal of Electrodeposited Multilayer Nanowires*, Thesis, Rensselaer Polytechnic Institute, Troy, New York, Pro Quest Information and Learning Company, UMI Microform 3286344, 2007.

Yuasa S., Djayaprawira D.D., *Giant Tunnel Magnetoresistance in Magnetic Tunnel Junctions with a Crystalline MgO(0 0 1) Barrier*, J. Phys. D: Appl. Phys., **40**, R337–R354 (2007).

CONTROLUL PARAMETRILOR UNOR SENZORI GMR CU VALVE DE SPIN PE BAZĂ DE ANTIFEROMAGNEȚI SINTETICI

(Rezumat)

A fost realizată o analiză simulațională a unei categorii particulare de antiferomagneți sintetici (AFS), utilizați la valvele de spin pentru senzorii GMR. Au fost considerate diferite structuri ale stivei de straturi în valva de spin, în scopul îmbunătățirii cuplajului antiferimagnetic puternic dintre stratul cu magnetizație fixată și stratul de referință (fabricate din aliaje magnetice dure de Co de tip Heusler), prin intermediul unui strat subțire separator (Ru, Ta, Ti). Au fost redate grafic reprezentări parametrice ale variației produsului rezistență - arie, ΔRA, precum și ale densității areale de stocare a biților, obținute pe baza considerațiilor teoretice și a simulărilor structurale folosind programul HFSS (tehnologie Ansoft). În cadrul modelului de simulare au fost considerate fenomenele interne și totodată influența câmpurilor externe. Se poate obține astfel o structură controlată, rezultatele noastre indicându-ne un raport MRG de circa 1.3...2.2%, pentru grosimi ale stratului separator de 0.8...1.2 nm, pentru o valoare a câmpului aplicat de circa 6...8 k Oe. Rezultatele depind de structura stivei, rolul fiecărui strat intermediar la nivelul căruia se manifestă interacțiuni de schimb fiind esențial în procesul de îmbunătățire a performațelor structurii.

BULETINUL INSTITUTULUI POLITEHNIC DIN IAŞI
Publicat de
Universitatea Tehnică „Gheorghe Asachi” din Iaşi
Volumul 62 (66), Numărul 4, 2016
Secţia
MATEMATICĂ. MECANICĂ TEORETICĂ. FIZICĂ

THE ACOUSTIC WORLD: MECHANICAL INERTIA OF WAVES

BY

ION SIMACIU*, ZOLTAN BORSOS, ANCA BACIU and GEORGETA NAN

Petroleum-Gas University of Ploieşti,
Department of Informatics, Information Technology, Mathematics and Physics (ITIMF)

Received: October 28, 2016
Accepted for publication: December 11, 2016

Abstract. In this paper, we analyze the phenomena that occur in a medium where the energy and information travels at the speed of mechanical waves. Disturbances are generated, evolves and propagates in the medium correlates with the acoustic waves (mechanical) having the maximum speed. The material environment and the disturbances that occur in it (waves, wave packets, bubbles, etc.) represents the acoustic world. We demonstrate that the wave has the equivalent mass. The equivalent mass of waves is linked to energy by an Einstein type relationship. Events in the acoustic world are linked by Lorentz type transformations. Studying the behavior of standing waves relative to an accelerated observer (Rindler observers) show that the equivalent mass of the wave is the inertial mass. For propagating waves, between linear momentum and generalized momentum (action variable) we find a de Broglie type relationship where the wave momentum is proportional to the wave number and the coefficient of proportionality is the action variable.

Keywords: mechanical waves; Rindler observers; equivalent mass of waves; de Broglie relation.

*Corresponding author; *e-mail*: isimaciu@yahoo.com

1. Introduction

For an electromagnetic universe, *i.e.* a universe those material systems and phenomena are correlated through electromagnetic waves and all events in different reference frames are linked by Lorentz transformations for inertial and by Rindler transformations for non-inertial systems. In the acoustic world, that universe where systems (waves, wave packets, bubbles, etc.) and mechanical phenomena are related by where events are linked by Lorentz type transformations for inertial and non-inertial systems Rindler type transformations. These transformations are obtained from the Lorentz and Rindler transformations replacing the speed of light c with speed of mechanical waves u. In the acoustic world, it was highlighted the existence of acoustic holes like black holes (gravitational and electromagnetic holes) (Unruh, 1995; Weinfurtner *et al*., 2013; Visser, 1998; Barceló *et al*., 2010; Barceló *et al*., 2011; Nandi *et al*., 2004). Observers from acoustic world have senses which are based on the perception of mechanical waves (any form of mechanical perturbation) and instruments that detect and acquire all information through the same type of wave (Nandi *et al*., 2004). Their measurements for time and length (and other parameters) are linked by Lorentz type transformations where the maximum speed is the speed of acoustic waves. Applying these transformations to the of standing waves packet, that energy, mass, linear and generalized momentum undergo relativistic changes.

In the second section, we calculate the energy of the wave that propagates in a fluid and the same calculations for standing wave. We calculate the macroscopic parameters of oscillators having a length equal to one half-wave (tube closed at both ends) or quarter wavelength (tube closed at one end and open at the other). For these oscillators, can define and calculate when generalized momentum (action variable) corresponding to the oscillation energy. The same parameters are calculated based on the constituent particles (atoms, molecules) energy and action.

In the third section, we express the energy as a function of the wave propagation speed. It highlights the existence of an equivalent mass of wave and Einstein type relation between energy and the mass. Also, the linear momentum of the wave (for wave that propagates) is defined. Between this linear momentum and generalized momentum (action variable) exist a de Broglie type relationship that is, the wave's momentum is proportional to the wave number, the coefficient of proportionality is the action variable.

The fourth section we study how to transform energy, mass, linear momentum and action variable of standing waves relative to an inertial observer and relative to a non-inertial observer. We highlight a rest mass and rest energy also a relativistic mass and energy (in inertial motion). Using Rindler type transformations, we show that the macroscopic oscillators equivalent mass is the inertial mass.

The fifth section the conclusions are presented.

2. Mechanical Waves

2.1. The Standing Wave in Gas

Consider a gas found in an tube-form enclosure with section $S = l_x l_y$ and length much greater than the transverse dimensions $l_z >> l_x, l_y$. The gas has the following properties: temperature *T*, pressure p_0, density ρ_0 and mass $m = \rho_0 S_{xy} l_z$. From a microscopic point of view, the gas is constituted of particles (atoms, molecules, etc.) with the mass m_a and density of the particles n_0 so the density is givenby $\rho_0 = n_0 m_a$.

The speed of propagation of mechanical waves in fluid is (Landau and Lifchitz, 1971, Ch. 8):

$$u = \sqrt{\left(\frac{\partial p}{\partial \rho}\right)_S} \tag{1}$$

For a gas, the wave propagation is an adiabatic process (constant entropy *S*) and $(\partial p/\partial \rho)_S$ can be expressed by adiabatic coefficient according to relationship

$$\left(\frac{\partial p}{\partial \rho}\right)_S = \frac{c_p}{c_V}\left(\frac{\partial p}{\partial \rho}\right)_V = \gamma\left(\frac{\partial p}{\partial \rho}\right)_V . \tag{2}$$

For a perfect gas, the speed becomes:

$$u = \sqrt{\frac{\gamma k_B T}{m_a}} . \tag{3}$$

If the tube is closed at both ends, there is created a longitudinal standing wave. The allowed modes are given by the expression of wave number (provided that the length of the rod to be equal to an integer of half-wavelength $l_z = j\lambda/2;\ j = 1,2,3,.....$)

$$k_j = j\frac{\pi}{l_z};\ j = 1,2,3,..... \tag{4}$$

From the definition of the wave phase velocity

$$u = \frac{\omega}{k}, \tag{5}$$

results the expression of angular frequency for mode *j*

$$\omega_j = u k_j = j\frac{\pi u}{l_z} . \tag{6}$$

The quantity

$$\omega_{\min} = \frac{\pi u}{l_z} = \frac{\pi u}{aN_z}. \tag{7}$$

is the minimum angular frequency corresponding mode $j = 1$.

The quantity

$$\omega_{\max} = \frac{\pi u}{l_z} = \frac{\pi u}{a} \tag{8}$$

is the maximum angular frequency corresponding mode $j = N_z$. In relations (7) and (8), the quantity a

$$a = n^{-3}. \tag{9}$$

is the average distance between gas particles at pressure p_0.

To the angular frequencies given by (7) and (8) correspond to the wavelength of maximum

$$\lambda_{\max} = 2l_z \tag{10}$$

and the minimum wavelength

$$\lambda_{\min} = 2a. \tag{11}$$

For a tube closed at one end, the length of the macroscopic oscillator is $\lambda/4$ because the modes are $l_z = (2j+1)\lambda/4;\ j = 0,1,2,3,\ldots$.

2.2. The Energy of Oscillation of the Standing Wave

For a longitudinal standing wave (Butikov, 2013), each element of length dz and mass $dm = \rho S dz$ executes an oscillatory movement and has kinetic energy ($\Psi_s(z,t) = q_{sz} = q_{0sz}\sin(kz)\sin(\omega t)$)

$$dE_k = \frac{1}{2}dm\left(\frac{\partial q_{sz}}{\partial t}\right)^2 = \frac{1}{2}dmq_{0sz}^2\omega^2\sin^2(kz)\cos^2(\omega t) \tag{12a}$$

and the potential energy

$$dE_p = \frac{1}{2}dmu_l^2\left(\frac{\partial q_{sz}}{\partial z}\right)^2 = \frac{1}{2}dmq_{0sz}^2\omega^2\cos^2(kz)\sin^2(\omega t). \tag{12b}$$

In the above relations, q_{sz} is instantaneous amplitude and q_{0sz} is maximum amplitude.

The total energy is

$$dE = dE_k + dE_p = \frac{1}{2}dmq_{0sz}^2\omega^2\left[\sin^2(kz)\cos^2(\omega t) + \cos^2(kz)\sin^2(\omega t)\right]. \tag{13}$$

With (13), the oscillation energy of the gas in the tube is

$$E=\frac{1}{2}\rho S q_{0sz}^2\omega^2\int_0^{l_z}\left[\sin^2(kz)\cos^2(\omega t)+\cos^2(kz)\sin^2(\omega t)\right]dz= \\ \frac{1}{4}\rho S l_z q_{0sz}^2\omega^2=\frac{1}{4}mq_{0sz}^2\omega^2. \tag{14}$$

For mode j, with $\lambda_j=2l_z/j$, the gas energy in the tube in standing wave mode is

$$E_j=\frac{j}{8}\rho l_x l_y q_{0szj}^2\omega_j^2\lambda_j=j\left(\frac{\lambda_j}{2}Sn\right)\left(\frac{1}{4}m_a q_{0szj}^2\omega_j^2\right)=jN_{\lambda_j/2}E_{aj} \tag{15}$$

with $N_{\lambda_j/2}$ the number of microscopic/atomic oscillators from a portion of the tube with length equal to a half-wave

$$N_{\lambda_j/2}=\frac{\lambda_j}{2}Snj \tag{16}$$

and

$$E_{aj}=\frac{1}{4}m_a q_{0szj}^2\omega_j^2 \tag{17}$$

the energy of a microscopic (atomic) oscillator.

Because the wavelength can be expressed by the speed of propagation u and pulsation ω_j

$$\lambda_j=\frac{2\pi u}{\omega_j}, \tag{18}$$

results, replacing in Eq. (15), the energy of the gas, as a macroscopic oscillator, is proportional to the angular frequency

$$E_j=j\left(\frac{\pi}{4}\rho S q_{0szj}^2 u\right)\omega_j=jJ_{\lambda_j/2}\omega_j\,. \tag{19}$$

From analytical mechanics (Fasano and Marmi, 2006, p. 431) the energy of the oscillator using harmonic coordinates (the action-angle variables) has the expression (19) where

$$J_{\lambda_j/2}=\left(\frac{\lambda_j}{2}Sn\right)\left(\frac{1}{4}m_a q_{0zj}^2\omega_j\right)=N_{\lambda_j/2}J_{aj} \tag{20}$$

it is generalized momentum (the canonical action variable) and

$$E_{\lambda_j/2}=\left(\frac{\pi}{4}\rho S q_{0szj}^2 u\right)\omega_j=J_{\lambda_j/2}\omega_j \tag{21}$$

is the macroscopic oscillator energy corresponding to a half-wavelength.

In Eq. (20), the parameter

$$J_{aj}=\frac{1}{4}m_a q_{0zj}^2\omega_j \tag{22}$$

is the generalized momentum (the canonical action variable) for microscopic (atomic) oscillator energy is given by (17).

For a given material, the oscillator energy and generalized momentum have the lowest value for thermal oscillations in solids, and thermal motion in fluids at temperature $T \neq 0\text{K}$.

The perturbations (the waves and waves packets formed through interference-diffraction) in this environment, an "acoustic world", are correlated with the maximum speed, the speed of waves in the environment. Oscillations produced in this material overlap these perturbations and thermal movements. In this world, the group velocity of the perturbations (the speed with which propagates the amplitudes) is less (or equal) than the speed of waves, $\upsilon = \upsilon_g \leq u$. It follows that the lowest values of generalized $J_{\min}$ momentum and energy $E_{\min}$

$$J_{\min} = J_{aT} = \frac{1}{2} m_a q_{0zT}^2 \omega_T , \tag{23}$$

$$E_{\min} = E_{aT} = \frac{1}{2} m_a q_{0zT}^2 \omega_T^2 \tag{24}$$

correspond to thermal oscillations for microscopic oscillators.

2.3. The Oscillation Energy of the Bar in Presence of a Wave

For a wave with frequency ω and the maximum amplitude q_{0z}, $\Psi(z,t) = q_z = q_{0z} \sin(\omega t - kz)$, which propagates in the gas founded in a tube (the tube has $l_z >> \lambda$), the tube can be considered as a system of oscillators of length $\lambda/2$. Using the same relations (12) and (13) for kinetic, potential and total energy of a half-wave is

$$E_{\lambda/2} = \left(\frac{\pi}{2} \rho S q_{0z}^2 u \right) \omega = J_{\lambda/2} \omega \tag{25}$$

and generalized momentum (the canonical action variable) is

$$J_{\lambda/2} = \frac{\pi}{2} \rho l_x l_y q_{0z}^2 u . \tag{26a}$$

or

$$2\pi J_{\lambda/2} = \pi^2 \rho S q_{0z}^2 u . \tag{26b}$$

The energy and the generalized momentum can be expressed as function of microscopic quantities: mass of atoms m_a and density n

$$E_{\lambda/2} = \left(\frac{\pi}{2} n m_a S q_{0z}^2 u \right) \omega = \left(nS \frac{\lambda}{2} \right) \left(\frac{\pi}{\lambda} m_a q_{0z}^2 u \omega \right) = N_{\lambda/2} E_a \tag{27}$$

$$J_{\lambda/2}=\left(nS\frac{\lambda}{2}\right)\left(\frac{\pi}{\lambda}m_a q_{0z}^2 u\right)=N_{\lambda/2}J_a, \tag{28}$$

with $N_{\lambda/2}$ - the number of atoms in the volume $V=S\lambda/2$, $E_a=\left(m_a q_{0z}^2\omega^2\right)/2=J_a\omega$ - the energy, $J_a=m_a q_{0z}^2\omega/2=\pi m_a q_{0z}^2 u/\lambda$ - the generalized momentum for microscopic/atomic oscillator given by the relations (17) and (22).

3. The Equivalent Mass of the Wave

3.1. The Mechanical Wave Mass

The macroscopic oscillator energy given by (25) can be expressed in terms of the velocity, considering the relation (5)

$$E_{\lambda/2}=\left(\frac{\pi}{2}\rho Skq_{0z}^2\right)u^2=\left(\pi^2\rho S\frac{q_{0z}^2}{\lambda}\right)u^2. \tag{29}$$

Introducing the notion of equivalent mass for a macroscopic oscillator corresponding to a half-wavelength

$$m_{u,\lambda/2}=\frac{\pi}{2}\rho Skq_{0z}^2=2\left(\rho S\frac{\lambda}{2}\right)\left(\frac{\pi q_{0z}}{\lambda}\right)^2=\frac{m_{\lambda/2}}{2}\left(\frac{2\pi q_{0z}}{\lambda}\right)^2, \tag{30}$$

with $m_{\lambda/2}=\rho S\left(\lambda/2\right)$ the mass of macroscopic oscillator's substance (gas), we can write an Einstein type expression for energy (Feynman *et al*., 1964, Ch. 15.9)

$$E_{\lambda/2}=m_{u,\lambda/2}u^2. \tag{31}$$

The linear momentum along the *Oz* direction corresponding to macroscopic oscillator, is

$$p_{z,\lambda/2}=m_{u,\lambda/2}u. \tag{32}$$

We can define also a linear momentum for wave, that is the root mean square of internal oscillation momentum (averaged over time and space) of atomic oscillators (usually, microscopic oscillators). From the momentum of an atomic oscillator

$$p_a=m_a\frac{\partial q_z}{\partial t}=m_a q_{0z}\omega\cos\left(\omega t-kz\right), \tag{33}$$

the root mean square atomic momentum is

$$P_a=\sqrt{\left\langle p_a^2\right\rangle_{z,t}}=\frac{1}{\sqrt{2}}m_a q_{0z}\omega. \tag{34}$$

The internal macroscopic momentum is the total momentum corresponding to the oscillators from a half-wavelength

$$P_{\lambda/2}=\left(nS\frac{\lambda}{2}\right)P_a=\sqrt{2}\left(\frac{\lambda}{2\pi q_{0z}}\right)m_{u\lambda/2}u=\sqrt{2}\left(\frac{\lambda}{2\pi q_{0z}}\right)p_{z\lambda/2} \tag{35a}$$

or

$$P_{\lambda/2}=\frac{1}{\sqrt{2}}\left(\frac{2\pi q_{0z}}{\lambda}\right)m_{\lambda/2}u_l \tag{35b}$$

and it is much higher than the wave momentum (32), for $\lambda >> q_{0z}$.

The ratio of the linear momentum of the oscillator (32) and action (26) is

$$\frac{p_{z,\lambda/2}}{J_{\lambda/2}}=k \tag{36}$$

a relationship between momentum and wave vector analogous to the photon (Bransden and Joachain, 1989, Ch. 1.3).

3.2. The Mass of Standing Wave

The j^{th} harmonics of standing wave in the gas-filled tube isa macroscopic oscillator corresponding to this tube is consisting of j half-wavelengthmacroscopic oscillators have, according to the relations (21) and (31), the energy

$$E_{\lambda_j/2}=\left(\frac{\pi}{4}\rho l_x l_y k_j q_{0szj}^2\right)u^2=\left(\frac{\pi^2}{2}\rho l_x l_y\frac{q_{0szj}^2}{\lambda_j}\right)u^2. \tag{37}$$

The equivalent mass, corresponding to this oscillator is

$$m_{us\lambda_j/2}=\frac{\pi^2}{2}\rho l_x l_y\frac{q_{0szj}^2}{\lambda_j}=\frac{m_{\lambda_j/2}}{4}\left(\frac{2\pi q_{0szj}}{\lambda_j}\right)^2. \tag{38}$$

Linear momentum along *Oz* direction and the total mean momentum are null.

For the standing wave, we can define an internal linear momentum as root mean square momentum (averaged over time and space) of atomic oscillators (usually, microscopic oscillators). The momentum of an atomic oscillator in the standing wave is

$$p_{aj}=m_a\frac{\partial q_{szj}}{\partial t}=m_a q_{0szj}\omega\sin(k_j z)\cos(\omega_j t). \tag{39}$$

Root mean square atomic momentum averaged in space and time is

$$P_{aj}=\sqrt{\left\langle p_{aj}^2\right\rangle_{z,t}}=\frac{1}{2}m_a q_{0szj}\omega_j. \tag{40}$$

The internal macroscopic momentum is the corresponding total momentum of oscillators from a half-wavelength

$$P_{\lambda_j/2}=\left(n\frac{\lambda_j}{2}l_x l_y\right)P_{aj}=\frac{1}{2}\left(\frac{\lambda_j}{\pi q_{0szj}}\right)\left(m_{us\lambda_j/2}u\right)=\left(\frac{2\pi q_{0szj}}{\lambda_j}\right)\left(m_{\lambda_j/2}u\right). \quad (41)$$

This momentum is different from expression (35) by the amplitude value ($q_{0szj}\neq q_{0z}$, for the standing wave with wavelength λ_j amplitudes are related by $q_{0szj}=2q_{0zj}$) of the wavelength $\lambda_j\neq\lambda$.

4. The Inertial Mass of Wave

4.1. The Standing Wave Relative to an Inertial Reference System

For an observer moving with constant velocity υ, the standing wave ($\Psi_s(z,t)=q_{sz}=q_{0sz}\sin(kz)\sin(\omega t)$) is an amplitude modulated waveform (Elbaz, 1986; Kracklauer, 1999)

$$\Psi(z,t)=q_{sz}=q_{0sz}\sin\left[\gamma_u k_0(z-\upsilon t)\right]\sin\left[\gamma_u\omega_0\left(t-\frac{\upsilon}{u^2}z\right)\right]. \quad (42)$$

The wave is characterized by: angular frequency

$$\omega=\gamma_u\omega_0>\omega_0, \quad (43)$$

the wave vector

$$k=\gamma_u k_0\frac{\upsilon}{u}<<k_0 \quad (43)$$

and the phase velocity

$$\upsilon_\varphi=\frac{\omega}{k}=\frac{u^2}{\upsilon}>>u. \quad (44)$$

The wave amplitude is modulated by: modulation frequency

$$\omega_{\text{mod}}=\gamma_u k_0\upsilon=\omega_0\gamma_u\frac{\upsilon}{u}<<\omega; \quad (45)$$

the wave vector

$$k_{\text{mod}}=\gamma_u k_0 \quad (46)$$

and group velocity equal to the speed of the observer

$$\upsilon_g=\frac{\omega_{\text{mod}}}{k_{\text{mod}}}=\upsilon<<u. \quad (47)$$

The amplitude of oscillation is modulated ($q_{\text{mod}}=q_{0sz}\sin\left[\gamma_u k_0(z-\upsilon t)\right]$) and the corresponding wavelength is

$$\lambda_{\text{mod}}=\frac{2\pi}{k_{\text{mod}}}=\frac{\lambda_0}{\gamma_u}<\lambda_0. \quad (48)$$

The relationships above are obtained using Lorentz transformations and Doppler displacement relations, replace the mechanical speed of light c with the mechanical wave propagation velocity u.

4.2. The Waves Relative to a Non-Inertial Referential System

To deduce the physical significance of the equivalent mass for wave given by Eq. (29), we deduce the expression of wave energy and mass relative to anaccelerated system.

Consider an accelerated reference frame $S'(x',y',z',t')$ characterized by acceleration vector $\vec{a}(0,0,a_z=a)$ relative to an inertial reference frame. The relations between z, t and proper time τ, relative to the reference frame instantly found the rest of the accelerated observer, Rindler observer (Rindler, 2006; Alsing and Milonni, 2004)

$$t(\tau)=\frac{u}{a}\sinh\left(\frac{a\tau}{u}\right),\quad z(\tau)=\frac{u^2}{a}\cosh\left(\frac{a\tau}{u}\right), \tag{49}$$

Relative to the reference frame being in instantly rest of the observer (the instantaneous rest frame of the observer) angular frequency ω' has the expression:

$$\omega'(\tau)=\frac{\omega-k\upsilon(\tau)}{\sqrt{1-\upsilon^2(\tau)/u^2}}=\omega\exp\left(\frac{-a\tau}{u}\right),\quad k=\frac{\omega}{u}, \tag{50a}$$

for waves that propagate towards the observer acceleration

$$\omega'(\tau)=\omega\exp\left(\frac{a\tau}{u}\right),\quad k=-\frac{\omega}{u} \tag{50b}$$

and for waves that propagate in the opposite direction of acceleration observer.

To deduce the half-wavelength energy corresponding to a wave (Eq. (25)) relative to the Rindler observers consider that the generalized impulse is Lorentz invariant

$$J'_{\lambda/2}=J_{\lambda/2}. \tag{51}$$

In those conditions, the expression of energy (25) transform same as pulsation (50)

$$E'_{\lambda/2}=J'_{\lambda/2}\omega'=J_{\lambda/2}\omega'. \tag{52}$$

Substituting (50) in the expression (52) gives

$$E'_{\lambda/2}=J_{\lambda/2}\omega\exp\left(\frac{a\tau}{u}\right)=E_{\lambda/2}\exp\left(\frac{a\tau}{u}\right). \tag{53}$$

The corresponding power relative to Rindler observer is

$$\mathrm{P}'_{\lambda/2}=\frac{dE'_{\lambda/2}}{d\tau}=E_{\lambda/2}\left(\frac{\mp a}{u}\right)\exp\left(\frac{\mp a\tau}{u}\right)=F'_{\lambda/2}u. \tag{54}$$

From the Eq. (54), results

$$F'_{\lambda/2} = \frac{E_{\lambda/2}}{u^2}(\mp a)\exp\left(\frac{\mp a\tau}{u}\right). \tag{55}$$

Substituting in (55), the expression of equivalent mass of the wave, according to the Eq. (30), gives

$$F'_{\lambda/2} = (\mp a)m_{u,\lambda/2}\exp\left(\frac{\mp a\tau}{u}\right) = (\mp a)m'_{u,\lambda/2}. \tag{56}$$

From Eq. (56), results that the inertial mass relative to the Rindler observer is dependent on proper time τ

$$m'_{u,\lambda/2}(a,\tau) = m_{u,\lambda/2}\exp\left(\frac{\mp a\tau}{u}\right). \tag{57}$$

and $m_{u,\lambda/2} = m'_{u,\lambda/2}(a=0)$, the inertial mass of the wave relative to the un accelerated observer $S(x,y,z,t)$, is the equivalent mass of the wave. It is observed that the equivalent mass wave has the same transformation expressions as energy and angular frequency.

5. Conclusions

The energy carried by a mechanical wave depending on the speed of propagation highlights the existence of an equivalent mass of wave. The two quantities are linked by an Einstein type relation. This mass is analogous with the mass of electromagnetic wave. The mechanical wave has also a linear momentum and an action which are connected by an analogous relation to the momentum and the wavelength of photon.

The standing wave is characterized by an energy and an equivalent rest mass connected by an Einstein type relation.

Relative to a moving observer the standing wave is a wave that carries energy with transport speed of reference frame in the opposite direction of movement. The relations between the quantities of the standing wave and progressive wave are Lorentz type transformations, the speed of light is replaced with the mechanical wave propagation speed in the medium. The relationship between energy and equivalent mass of progressive wave is Einstein type. The action corresponding to the standing wave has the same expression as progressive wave, *i.e.* it is invariant under Lorentz type transformations. The progressive wave momentum defined as the equivalent mass multiplied by the propagation velocity has a de Broglie type relation with invariant action.

Studying the behavior of standing wave compared with an accelerated reference frame (Rindler transformations), demonstrate that the equivalent mass of the wave is an inertial mass (a measure of mechanical inertia of system).

A substantial medium where propagates mechanical disturbances is an *acoustic universe* and the maximum energy and information propagation speed is the mechanical waves speed in undisturbed environment. All the phenomena that take place in this *acoustics world* are causally correlated with the same speed. The coordinate and time transformations between two coordinate frames are Lorentz type transformation. The results of this paper are developed in the papers (Simaciu *et al*., 2015; Simaciu *et al*., 2016).

REFERENCES

Alsing P.M., Milonni P.W., *Simplified Derivation of the Hawking-Unruh Temperature for an Accelerated Observer in Vacuum*, American Journal of Physics, **72** 1524-1529 (2004).

Barceló C., Garay L.J., Jannes G., *Two Faces of Quantum Sound*, Phys. Rev. D., **82**, *4*, 044042 (2010).

Barceló C., Liberati S., Visser M., *Analogue Gravity*, Living Rev. Relativity, **14**, 3-160 (2011).

Bransden B.H., Joachain Ch.J., *Introduction to Quantum Mechanics*, Longman Scientific & Technical (1989).

Butikov E.I., *Peculiarities in the Energy Transfer by Waves on Strained Strings*, Phys. Scr. 88 065402 doi:10.1088/0031-8949/88/06/065402 (2013).

Elbaz C., *Propriete cinematiques des particules materielles et des ondes stationnaires du champ*, Annales de la Fondation Louis de Broglie, Vol. **11**, No. *1*, pp. 65-84 (1986).

Fasano A., Marmi St., *Analytical Mechanics*, English translation, Oxford University Press (2006).

Feynman Richard P., Leighton R.B., Sands M., *The Feynman Lectures on Physics*, Vol. **1**, Addison-Wesley, Reading (1964).

Kracklauer A.F., *Pilot Wave Steerage: A Mechanism and Test*, Foundations of Physics Letters, Vol. **12**, No. *2*, 441-453 (1999).

Landau L., Lifchitz E., *Mecanique des fluids*, Edition Mir, Moscou (1971).

Nandi K.K., Zhangb Yuan-Zhong, Caic Rong-Gen, *Acoustic Wormholes*, arXiv:gr-qc/0409085v5 18 Nov (2004); K.K. Nandi, D.H. Xu, *Unruh model for the Einstein-Rosen charge: Squealing Wormholes?*, arXiv:gr-qc/0410052v2 13 Oct (2004).

Rindler W., *Relativity-Special*, General and Cosmological, Second Edition, Oxford University Press Inc., New York (2006).

Simaciu I., Borsos Z., Dumitrescu Gh., Nan G., *Planck-Einstein-de Broglie Relations for Wave Packet: The Acoustic World*, arXiv:1511.01049 (2015).

Simaciu I., Dumitrescu Gh., Borsos Z., Brădac M., *Interactions in an Acoustic World*, arXiv:1612.00294 (2016).

Unruh W.G., *Sonic Analog of Black Holes and the Effects of High Frequencies on Black Holes Evaporation*, Phys. Rev. D, **51**, 2827-2838 (1995).

Visser M., *Acoustic Black Holes: Horizons, Ergospheres and Hawking Radiation*, Class. Quantum Grav., **15**, 1767-1791 (1998).

Weinfurtner S. *et al*., *Classical Aspects of Hawking Radiation Verified in Analogue Gravity Experiment*, Lect. Notes Phys., **870**, 167-180 (2013); arXiv:1302.0375 [gr-qc].

LUMEA ACUSTICĂ: INERŢIA MECANICĂ A UNDELOR

(Rezumat)

În această lucrare analizăm fenomenele care se produc într-un mediu material în care energia şi informaţia se propagă cu viteza undelor mecanice. Perturbaţiile care se generează şi evoluează/propagă în mediu se corelează prin intermediul undelor acustice (mecanice) care au viteza maximă. Mediu material şi perturbaţiile care se produc în el (unde, pachete de unde, bule, etc.) formează lumea acustică. Noi demonstrăm că unda are masă echivalentă. Masa echivalentă este legată de energia undei printr-o relaţie de tip Einstein. Evenimentele din lumea acustică sunt legate prin transformări de tip Lorentz. Studiind comportarea unei unde staţionare în raport cu un observator accelerat (observatorul Rindler), demonstrăm că masa echivalentă a undei este masa inerţială. Pentru unda care se propagă, între impulsul liniar şi impulsul generalizat (action variable) există o relaţie de tip de Broglie adică impulsul undei este proporţional cu numărul de undă al undei, coeficientul de proporţionalitate fiind acţiunea.

BULETINUL INSTITUTULUI POLITEHNIC DIN IAŞI
Publicat de
Universitatea Tehnică „Gheorghe Asachi” din Iaşi
Volumul 62 (66), Numărul 4, 2016
Secţia
MATEMATICĂ. MECANICĂ TEORETICĂ. FIZICĂ

SIMULATING PHYSICAL PHENOMENA WITH MICROSOFT EXCEL

BY

ECATERINA AURICA ANGHELUŢĂ[1,*] and MIHAI DANIEL ANGHELUŢĂ[2]

[1] “Gheorghe Roșca Codreanu” National College, Bârlad
[2]“Iuliu Haţieganu” University of Medicine and Pharmacy, Cluj

Received: November 23, 2016
Accepted for publication: December 18, 2016

Abstract. The study presents a way to simulate certain physical phenomena, such as the composition of linearly harmonic oscillations or the polarization state of radiation, within Microsoft Excel. Those simulations aid the students to familiarize themselves with the graphical representation of the movement laws of a linear harmonic oscillator. Additionally, they can help in the study of special cases of coupling two linearly harmonic, either parallel or perpendicular, oscillations and in the understanding of ways to obtain different states of light polarization through the composition of several, conveniently out of phase, linearly polarized radiations.

Keywords: composition; oscillation; harmonic; light; polarization.

1. Introduction

“The Composition of Linearly Harmonic Oscillations” application window uses input data:

- Oscillations amplitude (A_1, A_2 in mm);
- Initial phases of the oscillations (in degrees);
- Oscillations period or pulse.

[*]Corresponding author; *e-mail*: ecaterinaangheluta@yahoo.com

Output data:

• Graphical representation of the oscillations $y_1(t)$, $y_2(t)$ and y_{rez} (equation of the resulting oscillation);

• Amplitude, oscillations phase offset, initial phase of the resulting oscillation.

2. Composition of Two Linearly Harmonic, Parallel Oscillations with Equal Frequencies

The application window allows for the study of composing two linearly harmonic, parallel oscillations with equal frequencies (Popescu *et al.*, 2006), for highlighting the special cases involving in-phase oscillations (Fig. 1*a*) with maximal value for the resulting amplitude, antiphase oscillations (Fig. 1*b*), with minimal value for the resulting amplitude, and the case of quadrature oscillations.

One can independently modify the values for oscillation amplitude and initial phase. Expressing the initial phase in degrees was preferred in order to be more suggestive for students and because was chosen a value of 1 degree for each incremental variation of the initial phase.

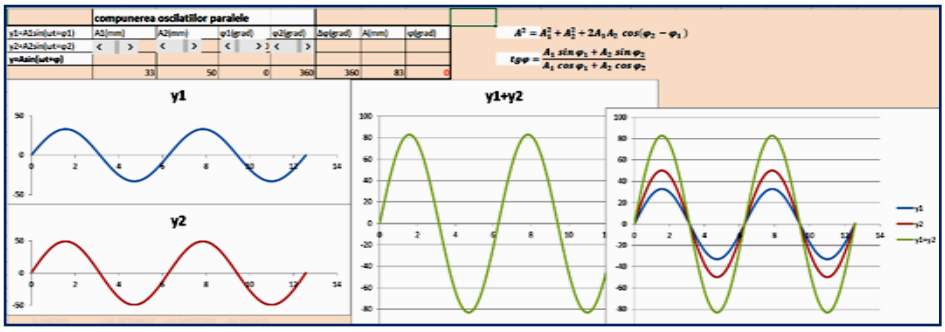

a

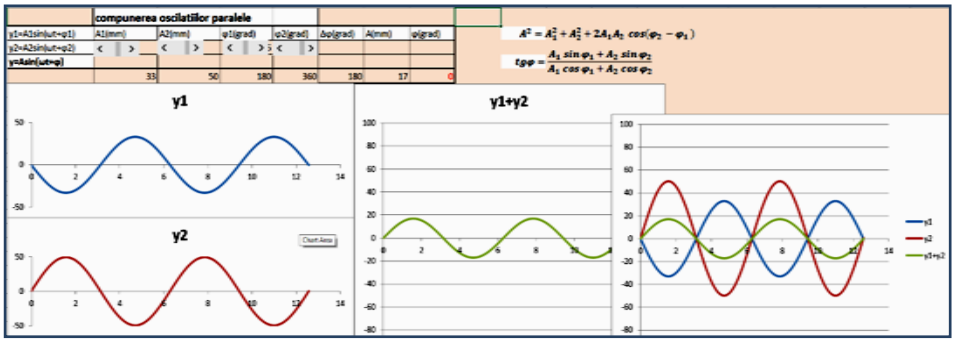

b

Fig. 1 – *a*) Combining two linearly harmonic, in-phase, parallel oscillations with equal frequencies, *b*) Combining two linearly harmonic, parallel, antiphase oscillations with equal frequencies.

3. Composition of Two Harmonic Oscillations of Different Frequencies Highlighting the Beat Phenomenon

Two linearly harmonic oscillations with the same amplitude and initial phase were graphically represented (Fig. 2). The periods and, consequently, the pulse of the oscillations can be modified. In the case of oscillations with the same pulse, we encounter the previous situation.

The students can now understand that the amplitude of the resulting oscillation is variable. The period increases with the decreasing of the difference between the pulse of the components. The resulting oscillation has a pulse equal to the mean of the two pulse values and a period much smaller than the one characterizing the variation in amplitude. One can now observe how the difference between the two pulse values can influence the aspect of the resulting oscillation.

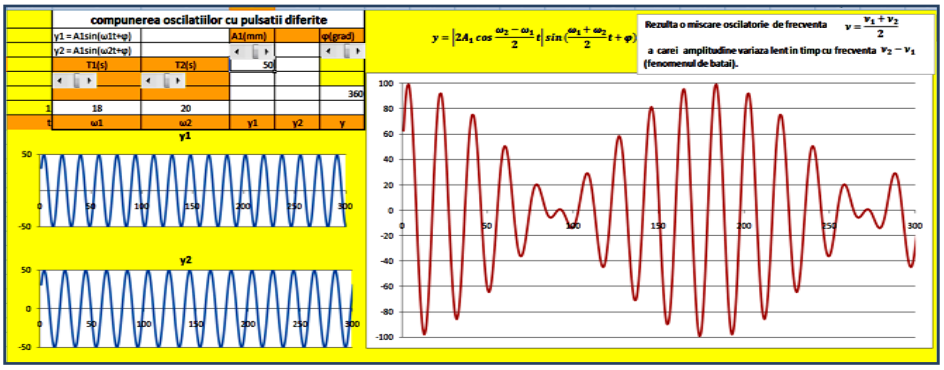

Fig. 2 – Combining two oscillations with different yet close pulse values – Highlighting the beat phenomenon.

4. Superposition of Perpendicular Harmonic Oscillations (the Lissajous Figures)

In this section two perpendicular oscillations, with modifiable amplitude and initial phase, were combined (Fig. 3). Additionally, the pulse values for these oscillations are not equal, being characterized by a proportionality relationship "*n*", where "*n*" can be either integral or fractional. The curves resulting from this situation are called the Lissajous figures. In Fig. 3, the trajectories corresponding to a few values for the proportionality relationship "*n*" were represented ($n = 1$, $n = 2$, $n = 6$).

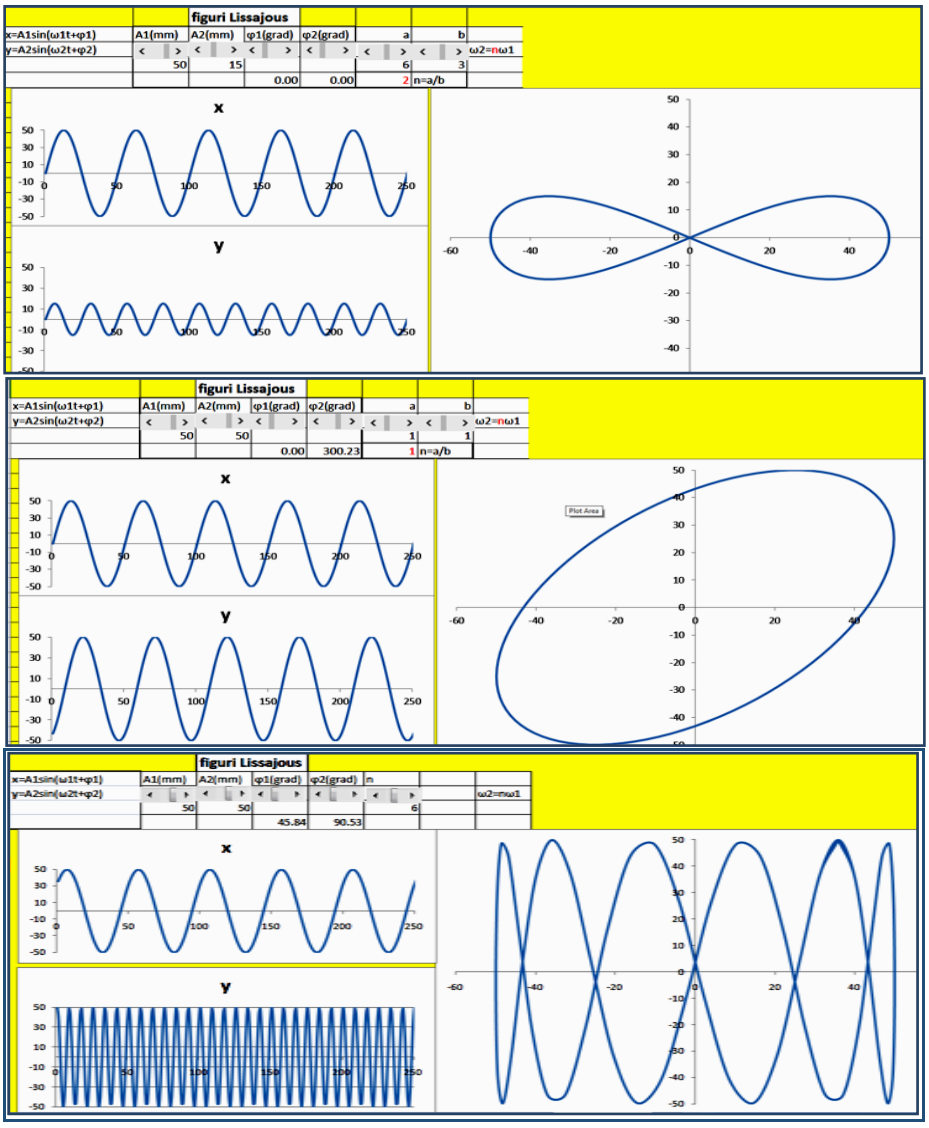

Fig. 3 – Combining two perpendicular oscillations (the Lissajous curves).

5. Application Description "Modelling the State of Polarization of Light"

The previous application allows for the modelling of the states of polarization of light, seenas a result of the composition of two perpendicular oscillations with equal pulse.

This approach is justified when the polarization of the light obtained through birefringence (Bruhat, 1965; Kužel, 2000/2001) consisting in the production of two refracted rays for each incident ray on an anisotropic crystal.

The two rays are polarized in perpendicular planes: in the ordinary ray, the oscillations of the electric field intensity occur perpendicularly to the main plane, while in the case of the extraordinary ray, the oscillations occur in a plane parallel to the main section one, as determined by the incident ray and the direction of the optic axis.

Should the propagation direction of the two rays be the optic axis, the two will have identical speed values, otherwise, the speeds differ. Due to the different speeds of propagation, a phase offset occurs between the two rays causing a change in the state of polarization for the radiation passing through a layer of anisotropic substance.

We will consider that the elliptical polarization corresponds to the general state of total polarized light. Depending on the values of the phase offset δ, the states of polarization for totally polarized radiations can be obtained as special cases of elliptical polarization (Table1).

Table 1
Polarization States of Electromagnetic Radiations in Relation with the Phase Offset Value

Nr.crt.	Phase offset value	State of polarization
1.	$\delta = \delta_y - \delta_x = m\pi$, m = 0, 1, …	Linear
2.	$\delta = \delta_y - \delta_x = \pm \pi/2$ $E_{0y} = E_{0x}$	Circular
3.	$\delta \in (0, \pi)$	Right elliptical
	$\delta \in (\pi,\ 2\pi)$	Left elliptical
	$\delta = \pm\pi / 2$	Elliptical the axes of the ellipse coincide with the Ox and Oy axes.

The states of polarization can be represented with the help of the Stokes parameters (Guenther, 1990). In the ideal case of a plane, fully polarized, monochromatic wave, the matrix of the normalized Stokes parameters can be expressed in relation to ψ (tg ψ = E_{0x}/E_{0y}, where E_{0x} and E_{0y} are the electric field intensity amplitudes for the two perpendicular oscillations) and δ according to Eq. (1).

$$\begin{pmatrix} s_0 \\ s_1 \\ s_2 \\ s_3 \end{pmatrix} = \begin{pmatrix} 1 \\ -\cos 2\psi \\ \sin 2\psi \cos\delta \\ \sin 2\psi \sin\delta \end{pmatrix} \tag{1}$$

For a linearly polarized, incident radiation that propagates perpendicularly to the optic axis of an anisotropic uniaxial medium, an Excel application was developed to allow for the modification of the phase offset between the ordinary and the extraordinary rays and also, to obtain the different states of polarization for the emerging radiation.

In order to modify the phase, offset values of the two oscillations an increment/decrement button type form controller was added. In the application window the electric field intensity oscillations on the two perpendicular axes Ox and Oy (the directions of the neutral lines of the anisotropic medium) and the shape of the oscillation resulting from the combination of the two, were illustrated (Figs. 5-7).

The application also allows for the determination of the Stokes vectors for each state of polarization. The vector elements can be placed with the desired precision.

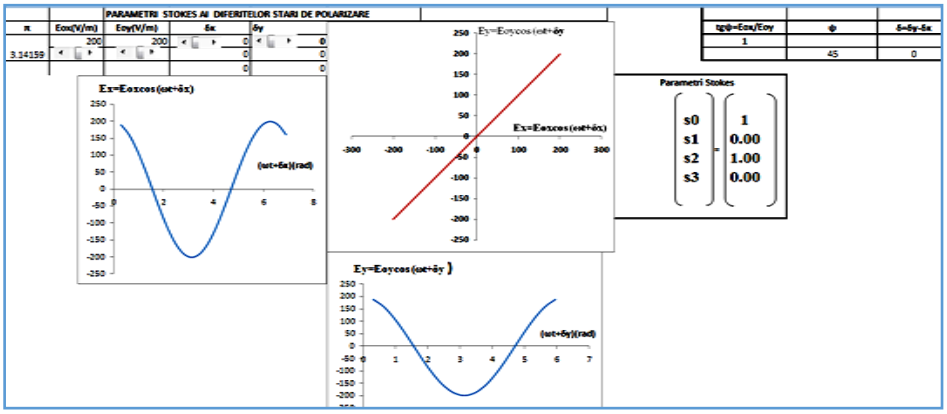

Fig. 4 – Linearly polarized radiation orientated at a 45° angle in relation with the XOY coordinate system.

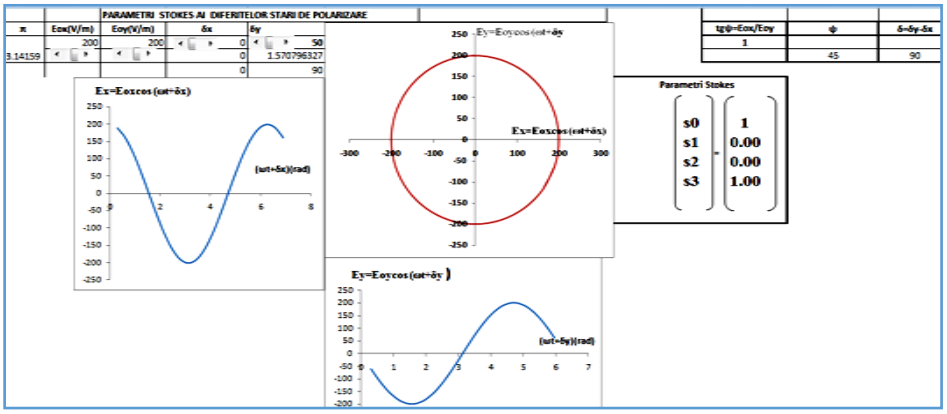

Fig. 5 – Circularly polarized right radiation.

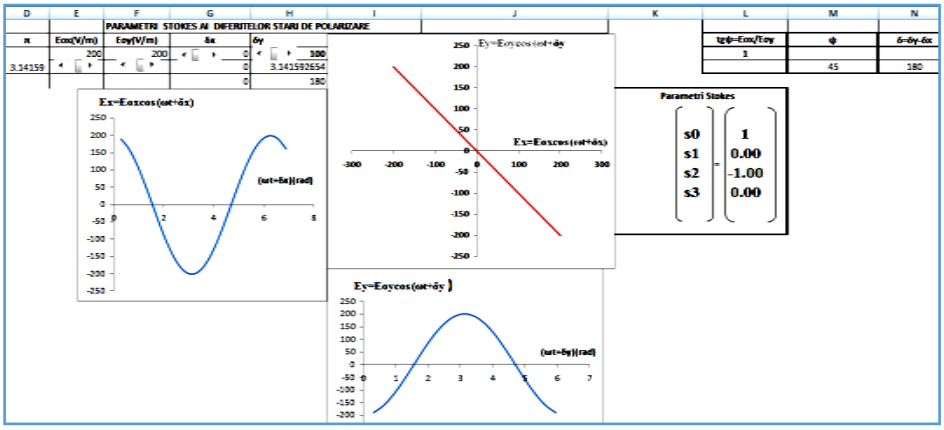

Fig. 6 – Linearly polarized radiation with modified azimuth.

6. Conclusions

Simulating and modelling physics phenomena, that are difficult to recreate in the school laboratory, with the help of computer software helps the students to better understand and broaden their knowledge of the phenomena while transforming the computer into a virtual lab.

REFERENCES

Bruhat G., *Cours de physique generale, optique*, Masson Paris, 1965.
Guenther Robert D., *Modern optics*, Duke University, John Wiley & Sons, 38-49, 1990.
Kužel P., *Electromagnétisme des milieuxcontinus - OPTIQUE* - Licence de Physique, Institut Galilée, Université Paris-Nord 2000/2001, 31-38.
Popescu M., Tomescu V., Strazzaboschi S., SanduM., *Fizică, manual pentru clasa a XI-a*, Edit. Crepuscul, 2006.

SIMULAREA UNOR FENOMENE FIZICE CU AJUTORUL APLICAȚIEI MICROSOFT EXCEL

(Rezumat)

Studiul prezintă modul în care pot fi simulate unele fenomene fizice, precum compunerea oscilaţiilor liniar armonice sau starea de polarizare a radiaţiilor, în aplicaţia Microsoft Excel. Simulările îi ajută pe elevi: să se familiarizeze cu interpretarea grafică a legilor de mişcare pentru un oscillator liniar armonic, să studieze cazuri de interes pentru compunerea a două oscilaţii liniar armonice paralele sau perpendicular şi să înţeleagă cum se pot obţine diferite stări de polarizare a luminii prin compunerea unor radiaţii liniar polarizate defazate convenabil.

BULETINUL INSTITUTULUI POLITEHNIC DIN IAŞI
Publicat de
Universitatea Tehnică „Gheorghe Asachi” din Iaşi
Volumul 62 (66), Numărul 4, 2016
Secţia
MATEMATICĂ. MECANICĂ TEORETICĂ. FIZICĂ

NON-STANDARD ANALYSIS AND NON-DIFFERENTIABILITY

BY

IRINEL CASIAN BOTEZ*

“Gheorghe Asachi” Technical University of Iaşi,
Faculty of Electronics, Telecomunication and Information Technology

Received: November 23, 2016
Accepted for publication: December 20, 2016

Abstract. In this article we demonstrate the link between fractal features and nediferentiabilitate.

Keywords: Non-standard model of arithmetic; representation theory.

1. Introduction

In 1821 Cauchy defines the infinitesimals as follows, I quote in French: “On dit qu’une quantité variable deviant *infiniment petite*, lorsque sa valeur numérique décroit indéfiniment de manière à converger vers la limite zéro” (Cauchy, 1821, p. 29). It is good to note that there is a difference between the concepts of *constant decline* and *fall unlimited*. Thus, a variable admitting that successive terms from the following string (Cauchy, 1821):

$$\frac{2}{1},\frac{3}{2},\frac{4}{3},\frac{5}{4},\frac{6}{5},\ldots \tag{1}$$

extended indefinitely, steadily decreases, but not unlimited, because successive values converge to limit 1. On the other hand, a variable admitting that successive terms from the following string (Cauchy, 1821):

*Corresponding author; *e-mail*: icasian@etti.tuiasi.ro

$$\frac{1}{4},\frac{1}{3},\frac{1}{6},\frac{1}{5},\frac{1}{8},\frac{1}{7},\ldots \tag{2}$$

extended indefinitely, steadily decreases, because the difference between two consecutive terms of this sequence is, alternative, positive and negative; however, the variable decreases unlimited because its values could be made smaller than any given number.

2. Are the Infinitesimals Real Numbers?

The Cauchy's definition of infinitesimals is an intuitive one. Hilbert, in his formal approach to mathematics, is not interested in the question "*what are certain structures?*" but "*what are these properties and what can be deduced from these properties*". Thus, a more accurate definition of the infinitesimals would be: an infinitesimal ε is an element of an ordered field K, nonzero, which has the property:

$$-r < \varepsilon < r \tag{3}$$

whatever positive real number r. It is essential now to mention that any nonzero real number does not check the Eq. (3), so an infinitesimal is not a real number. So, the field should be viewed as an extension of the field $\mathbb{R}$ of the orderly real numbers. This field we call of *hyper-real numbers*, and we will note it by ${}^{*}\mathbb{R}$. It is demonstrated (Robinson, 1996) that a finite number k can be put in the form $c+\varepsilon$, where c is a real number, and ε is either zero or an infinitesimal. The real number c is called the standard part of the finite number k, which is written as:

$$\mathrm{c} = \mathrm{st}\left[\mathrm{k}\right] \tag{4}$$

We have been encountered such situations in mathematics. The irrational numbers were introduced in order to solve certain equations. The complex numbers were created by insertion of the ideal item $\sqrt{-1}$. The novelty of the situation with which we are dealing was noted in by Felix Klein. He remarks in Volume 1 of his book (Klein, 1932) that we are dealing with two theories of continuum:

• continuum A (A from Archimedes), illustrated mathematically by the set of real numbers.

• continuum B (B from Bernoulli), mathematical exemplified by what Robinson called *hyperreal numbers*. A possible explanation for the relationship between the two continuums follows. All values from continuum A are (theoretically) possible to be results of measurements. Continuum B has values like $x+dx$ that can never be the reading of measurements.

3. Does it can be Defined the Derivative without Using the Limit?

Leibniz's definition of differential quotient, $\Delta y/\Delta x$, whose logic weakness was criticized by Berkeley, it was amended by Robinson using standard application part, denoted by "st", defined on the continuum B with values in continuum A. With $f(x)$ a function which has values in ${}^{*}\mathbb{R}$ and $a < x_0 < b$, where $x_0 \in \mathbb{R}$, we say that it is *differentiable of order 1* if and only if there is a standard real number c for which:

$$f(x) - f(x_0) \simeq c(x - x_0) = c\varepsilon \tag{5}$$

For any $x \neq x_0$ from the monad of x_0 (Robinson, 1996). The standard real number *c* is named, in this case, the derivative of order 1 of $f(x)$, in x_0 and is denoted by $f^{(1)}(x_0)$ or $f'(x_0)$. So, the derivative can be defined using the *standard part* function:

$$f^{(1)}(x_0) = st\left[\frac{f(x_0+\varepsilon) - f(x_0)}{\varepsilon}\right] \tag{6}$$

where all infinitesimals ε are of order 1 (Robinson, 1996).

4. Conclusions

If expression (6) is constant and independent of ε, f is a differentiable function. But if it is not, Eq. (6) is dependent of infinitesimals ε, which demonstrate that, geometrically, the recommended choice to deal with is a fractal function, $F(x,\varepsilon)$, which depends on ε, but which converge to $f(x)$ when $\varepsilon \to 0$.

REFERENCES

Cauchy M.A.-L., *Cours D'Analyse De L'Ecole Royale Plytechnique*, DEBURE Freres, Libraires du Roi et de la Bibliotheque du Roi (1821).

Klein F., *Elementary Mathematics*, Macmillan And Company Limited (1932).

Robinson A., *Non-standard Analysis*, Princeton, New Jersey, Princeton University Press (1996).

ANALIZA NON-STANDARD ȘI NE-DIFERENȚIABILITATE

(Rezumat)

În acest articol demonstrăm legătura dintre funcțiile fractale și nediferențiabilitate.